Monthly Notices
of the
ROYAL ASTRONOMICAL SOCIETY

MNRAS **454,** 419–438 (2015) doi:10.1093/mnras/stv1881

Cold dust emission from X-ray AGN in the SCUBA-2 Cosmology Legacy Survey: dependence on luminosity, obscuration and AGN activity

Manda Banerji,[1,2★] R. G. McMahon,[1,2] C. J. Willott,[3] J. E. Geach,[4] C. M. Harrison,[5] S. Alaghband-Zadeh,[1] D. M. Alexander,[5] N. Bourne,[6] K. E. K. Coppin,[4] J. S. Dunlop,[6] D. Farrah,[7] M. Jarvis,[8,9] M. J. Michałowski,[6] M. Page,[10] D. J. B. Smith,[4] A. M. Swinbank,[5] M. Symeonidis[10] and P. P. van der Werf[11]

[1]*Institute of Astronomy, University of Cambridge, Madingley Road, Cambridge CB3 0HA, UK*
[2]*Kavli Institute for Cosmology, University of Cambridge, Madingley Road, Cambridge CB3 0HA, UK*
[3]*Herzberg Institute of Astrophysics, National Research Council, 5071 West Saanich Rd, Victoria, BC V9E 2E7, Canada*
[4]*Centre for Astrophysics Research, University of Hertfordshire, College Lane, Hatfield, Hertfordshire AL10 9AB, UK*
[5]*Centre for Extragalactic Astronomy, Department of Physics, Durham University, South Road, Durham DH1 3LE, UK*
[6]*Institute for Astronomy, University of Edinburgh, Royal Observatory, Blackford Hill, Edinburgh EH9 3HJ, UK*
[7]*Department of Physics, Virginia Tech, Blacksburg, VA 24061, USA*
[8]*Oxford Astrophysics, Department of Physics, Keble Road, Oxford OX1 3RH, UK*
[9]*Physics Department, University of the Western Cape, Bellville 7535, South Africa*
[10]*Mullard Space Science Laboratory, University College London, Holmbury St Mary Dorking, Surrey RH5 6NT, UK*
[11]*Leiden Observatory, Leiden University, PO Box 9513, NL-2300 RA Leiden, the Netherlands*

Accepted 2015 August 12. Received 2015 July 29; in original form 2015 May 5

ABSTRACT

We study the 850-µm emission in X-ray-selected active galactic nuclei (AGN) in the $\sim$2 deg^2 COSMOS field using new data from the SCUBA-2 Cosmology Legacy Survey. We find 19 850-µm bright X-ray AGN in a 'high-sensitivity' region covering 0.89 deg^2 with flux densities of $S_{850} = 4$–10 mJy. The 19 AGN span the full range in redshift and hard X-ray luminosity covered by the sample – $0.7 \lesssim z \lesssim 3.5$ and $43.2 \lesssim \log_{10}(L_{\rm X}) \lesssim 45$. We report a highly significant stacked 850-µm detection of a hard X-ray flux-limited population of 699 $z > 1$ X-ray AGN – $S_{850} = 0.71 \pm 0.08$ mJy. We explore trends in the stacked 850-µm flux densities with redshift, finding no evolution in the average cold dust emission over the redshift range probed. For type 1 AGN, there is no significant correlation between the stacked 850-µm flux and hard X-ray luminosity. However, in type 2 AGN the stacked submillimeter flux is a factor of 2 higher at high luminosities. When averaging over all X-ray luminosities, no significant differences are found in the stacked submillimeter fluxes of type 1 and type 2 AGN as well as AGN separated on the basis of X-ray hardness ratios and optical-to-infrared colours. However, at $\log_{10}(L_{2-10}/{\rm erg\ s^{-1}}) > 44.4$, dependences in average submillimeter flux on the optical-to-infrared colours become more pronounced. We argue that these high-luminosity AGN represent a transition from a secular to a merger-driven evolutionary phase where the star formation rates and accretion luminosities are more tightly coupled. Stacked AGN 850-µm fluxes are compared to the stacked fluxes of a mass-matched sample of K-band-selected non-AGN galaxies. We find that at $10.5 < \log_{10}(M_*/{\rm M_\odot}) < 11.5$, the non-AGN 850-µm fluxes are 1.5–2 times higher than in type 2 AGN of equivalent mass. We suggest these differences are due to the presence of massive dusty, red starburst galaxies in the K-band-selected non-AGN sample, which are not present in optically selected catalogues covering a smaller area.

Key words: quasars: general – X-rays: galaxies – galaxies: evolution – submillimetre: galaxies.

1 INTRODUCTION

Studying the connection between star formation in galaxies and accretion on to the supermassive black hole is of prime importance

---

★ E-mail: mbanerji@ast.cam.ac.uk

Published by Oxford University Press on behalf of the Royal Astronomical Society

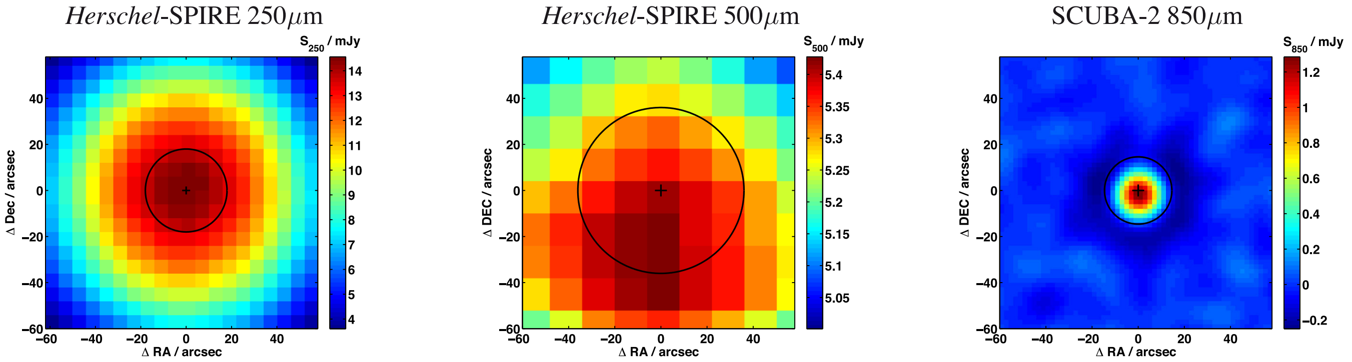

Figure 1. Stacked 250 μm (left), 500 μm (middle) and 850 μm (right) images of 2865 radio sources in the COSMOS field from Schinnerer et al. (2010). The superior spatial resolution and angular scale of the SCUBA-2 data is apparent relative to *Herschel*. For the 850-μm stack, we confirm that the peak emission is clearly coming from the central pixels demonstrating that the astrometry of the maps is accurate at the sub-pixel level. The negative 'bowling' around the bright central source seen in the SCUBA-2 850-μm image, is an artefact of the filtering procedure employed to generate the map.

in understanding galaxy formation (e.g. see Alexander & Hickox 2012 for a recent review). The discovery that supermassive black holes are ubiquitous with their mass connected tightly to the stellar bulge mass of galaxies (Magorrian et al. 1998; Kormendy & Ho 2013) has led to the realization that these active galactic nuclei (AGN) play a fundamental role in regulating the growth of galaxies. Sophisticated galaxy formation simulations now incorporate feedback from the AGN, which is shown to be critical in order to explain the observed numbers of massive galaxies (e.g. Di Matteo, Springel & Hernquist 2005; Springel, Di Matteo & Hernquist 2005; Croton et al. 2006). In these simulations, massive galaxies are assembled through gas-rich mergers which induce luminous bursts of obscured star formation. Star formation and black hole accretion are fuelled by a common gas supply and the star formation is initially dust obscured. As the gas and dust are expelled from the galaxy e.g. via AGN-driven winds, the accreting black hole emerges as an X-ray/UV luminous quasar. In such a picture of galaxy formation, luminous starburst galaxies, obscured and unobscured AGN are linked through a well-defined evolutionary sequence. Within unified AGN models (Antonucci 1993; Urry & Padovani 1995), the obscuration of the central accreting source can also be explained purely as a result of orientation effects and the distinction between unobscured type 1 AGN and obscured type 2 AGN is attributed to the line of sight through which they are viewed.

Obscuration in AGN almost certainly results from a combination of orientation and evolution driven factors. One way to distinguish between these is to look for evidence for obscured AGN having excess star formation in their host galaxies relative to their unobscured counterparts. Several early studies of X-ray luminous AGN using the SCUBA bolometer on the James Clerk Maxwell Telescope (JCMT) showed this to be the case (Page et al. 2001, 2004; Stevens et al. 2005). More recently, new data at far-infrared wavelengths from the *Herschel* Space Observatory, has been used to study the connection between star formation in galaxies and accretion on to the central AGN (e.g. Lutz et al. 2008; Shao et al. 2010; Bonfield et al. 2011; Harrison et al. 2012; Mullaney et al. 2012; Page et al. 2012; Rosario et al. 2012; Rovilos et al. 2012; Santini et al. 2012; Azadi et al. 2014; Stanley et al. 2015). Lutz et al. (2010) have also conducted a study of the 870-μm properties of $z \sim 1$ AGN using LABOCA. There is now a growing consensus that moderate-luminosity AGN tend to occupy star-forming host galaxies and that the star formation rate (SFR) is independent of AGN X-ray luminosity in this regime. AGN activity in galaxies occurs on very different spatial as well as temporal scales relative to star formation, which means that the instantaneous SFR in galaxies is unlikely to be tightly coupled to the instantaneous accretion rate (Hickox et al. 2014). However, at high luminosities, major merger-driven evolution can lead to a tighter coupling between AGN activity and star formation.

Studying the connection between star formation and AGN activity at high luminosities requires multiwavelength data from the X-ray to submillimeter wavelengths over reasonably wide fields. The COSMOS field is among the most well-studied extragalactic fields with a plethora of multiwavelength photometric and spectroscopic data. X-ray data is available from both the *XMM–Newton* and *Chandra* observatories and the field has been imaged at many other wavelengths, in particular with *Spitzer* and *Herschel*. Moreover, the wide area covered by many of these data sets now provides crucial information for the most luminous, high-redshift galaxies and AGN. Recently, the SCUBA-2 bolometer on the JCMT has provided a submillimeter map at 850 μm over the entire 2 $\deg^2$ field as part of the SCUBA-2 Cosmology Legacy Survey (S2CLS; Geach et al. 2013). The 850-μm data offers several advantages over *Herschel* observations over the same region. First, the superior angular resolution and smaller beam size relative to *Herschel* mean that source blending is less of an issue when inferring the average submillimeter properties of AGN (see Fig. 1). Secondly, the negative k-correction at these wavelengths at $z > 1$ (Blain et al. 2002), ensures that we are sensitive to roughly constant dust luminosity for essentially all high redshift galaxies in an 850-μm flux-limited sample. Furthermore, even in the *Herschel*-SPIRE bands, there can be a significant contribution from AGN dust heating in the case of the most luminous quasars (e.g. Rosario et al. 2012). The submillimeter dust emission at 850 μm is much less prone to such contamination from the AGN. Although it could potentially be more contaminated by synchrotron emission, this is unlikely to be an issue for the majority of AGN which are radio quiet The dust emission at 850 μm can therefore more safely be attributed to heating by star formation. At shorter wavelengths, it becomes necessary to disentangle the relative contributions of starburst and AGN heating to the total infrared flux and linking the two phenomena is therefore more complicated, with potential biases arising to derived SFRs due to different assumptions regarding the intrinsic AGN model.

The aim of this paper is to study the 850-μm properties of both unobscured (type 1) and obscured (type 2) AGN in the COSMOS field where statistically significant numbers of these populations now exist. We look for dependences of this submillimeter emission on the AGN host galaxy properties and compare to non-AGN galaxies. As such, our analysis is intended to provide the first S2CLS 850-µm view of the X-ray AGN population at high redshift. Throughout this paper, we assume a flat concordance cosmology with $H_0 = 70$ km s^{-1} Mpc^{-1}.

2 DATA

2.1 SCUBA-2 850 µm

Our primary data set used in this analysis is the SCUBA-2 850-µm map in the COSMOS field obtained as part of the S2CLS (Geach et al. 2013). The wide-field map covers a total area of ∼2 deg^2 imaged using a 4×45 arcmin PONG scanning pattern. The basic principle of the data reduction is to extract astronomical signal from the time-streams recorded by each bolometer in the SCUBA-2 array and map them on to a two-dimensional celestial projection. We have used the Dynamical Iterative Map-Maker (DIMM) within the *Sub-Millimetre Common User Reduction Facility* (SMURF; Chapin et al. 2013). We refer readers to Chapin et al. (2013) for a detailed overview of SMURF, and detailed data reduction steps will be given in Geach et al. (in preparation) but describe the main steps here.

Flat-fields are applied to the time-streams using flat scans that bracket each observation, and a polynomial baseline fit is subtracted from each bolometer's time-stream. Each time-stream is cleaned for spikes and DC steps are removed and gaps filled. After cleaning, the DIMM enters an iterative process that aims to fit the data with a model comprising a common mode signal, astronomical signal and noise. Next, a filtering step is performed in the Fourier domain, which rejects data at frequencies corresponding to angular scales $\theta > 150$ arcsec and $\theta < 2$ arcsec. The next step is to estimate the astronomical signal, which is subtracted from the data. Finally, a noise model is estimated for each bolometer by measuring the residual, which is then used to weight the data during the mapping process in additional steps. The iterative process above runs until convergence is met. In this case, we execute a maximum of 20 iterations, or when the map tolerance reaches 0.05.

The final 850-µm map in the COSMOS field has non-uniform depth with typical rms values of σ_{850} ∼2 mJy in one half, σ_{850} ∼4 mJy in the other half and σ_{850} ∼1 mJy in the central region. An 850-µm catalogue containing 360 sources has been produced from this map by searching for all sources above 3.5σ in regions with $\sigma_{850} < 2$ mJy (Geach et al. in preparation). This 850-µm catalogue covers an area of 0.89 deg^2. Our search for AGN that are individually detected at 850 µm covers this smaller area, higher sensitivity region. However, when studying the stacked properties of the AGN, we utilize the full area in order to get the largest AGN samples possible. As stacked fluxes are weighted by the noise (see Section 4), AGN in lower rms regions are automatically downweighted when calculating average 850-µm fluxes.

We begin by checking the astrometry of this 850-µm map by stacking a sample of 2865 radio sources in the COSMOS field (Schinnerer et al. 2010) in this map. The stacking procedure is described in more detail in Section 4 and the stacked 850-µm image for these radio sources is shown in Fig. 1. The peak 850-µm emission has an offset of 1.4 arcsec relative to the radio position. The SCUBA-2 850-µm pixel scale is 2 arcsec. This confirms that the maps have the correct astrometry at the sub-pixel level and can therefore be used in our stacking analysis. We also show the stacked images of the same radio sources in the *Herschel*-SPIRE 250- and 500-µm bands in Fig. 1. The *Herschel*-SPIRE data in the COSMOS field is taken from the *Herschel* Multi-tiered Extragalactic Survey (Oliver et al. 2012). Maps have been produced using the Level 2 data products from the ESA archive as detailed in Swinbank et al. (2014). While the stacked 250-µm emission appears to be well centred at the radio position, the 500-µm emission shows an offset relative to the radio position. The superior spatial resolution and pixel scale of the SCUBA-2 data relative to *Herschel*-SPIRE, are clearly apparent in this plot. The longer wavelength SCUBA-2 850-µm observations are therefore extremely complementary to already published *Herschel* observations of AGN in this field.

2.2 AGN catalogue

The aim of this paper is to study the submillimeter properties of a statistically significant and homogenous sample of AGN. The COSMOS field (Scoville et al. 2007) provides the largest and most well-characterized AGN sample overlapping the new SCUBA-2 CLS data. The AGN parent sample is a catalogue of *XMM–Newton*-detected X-ray point sources, which goes down to a flux limit of 9.3e-15 erg s^{-1} cm^{-2} in the 2–10 keV band over 90 per cent of the area. The flux limit for the faintest sources detected in the catalogue are 5e-16 erg s^{-1} cm^{-2} and 2.5e-15 erg s^{-1} cm^{-2} in the 0.5–2 keV and 2–10 keV bands, respectively. We only consider X-ray sources with robust multiwavelength optical and infrared cross-identifications from Brusa et al. (2010), which corresponds to ∼98 per cent of the X-ray sources. We make use of the latest spectroscopic and photometric redshifts for these AGN (Salvato et al. 2011; Bongiorno et al. 2012) together with the corresponding spectroscopic and photometric classifications.[1] The type 1 and type 2 samples specifically constitute AGN with broad emission lines in the case of the spectroscopic type 1s and narrow emission lines in the case of the spectroscopic type 2s. For the AGN with photometric redshifts, type 1 AGN are considered to be those fit by templates 19–30 in Salvato et al. (2011) whereas type 2 AGN are those fit by templates 1–18 or >100 (which correspond to galaxy templates). The photometric redshift accuracy is in general very good $\sigma_{\Delta z}/(1+z) = 0.014$ for $i_{\rm AB} < 22.5$ and 0.015 for $i_{\rm AB} < 24.5$ (Salvato et al. 2009). Photometry at mid-infrared wavelengths is from the *Spitzer* S-COSMOS Survey (Sanders et al. 2007). There are a total of 1797 AGN with multiwavelength cross-identifications in these catalogues. The observed hard-band (2–10 keV) X-ray luminosity versus redshift for both the type 1 and type 2 AGN can be seen in Fig. 2. These X-ray luminosities have been calculated from the hard-band fluxes from Brusa et al. (2010) assuming a photon index of $\Gamma = 1.8$. In the case of the type 1 AGN that are detected in the soft (0.5–2 keV) band but not in the hard band, the soft X-ray fluxes from Brusa et al. (2010) are used to estimate the hard X-ray flux, once again assuming $\Gamma = 1.8$. We note that no absorption correction has been applied to these luminosities as the X-ray data for the entire sample is in general of insufficient quality to allow full spectral fitting. The type 1 AGN have negligible absorption and in the case of the type 2 COSMOS AGN that are detected in the hard X-ray, Lusso et al. (2011) estimate the average shift in the hard X-ray luminosity introduced by an absorption correction to be $<\Delta\log(L_{2-10})>= 0.04 \pm 0.01$. In Appendix A, we compare the hard X-ray luminosities derived in this paper to those derived by Brightman et al. (2014) for a subset of the COSMOS AGN with *Chandra* data and where complex absorption spectral models can be fit, demonstrating that there are no significant biases in the X-ray luminosities used in this paper.

---

[1] http://www2011.mpe.mpg.de/XMMCosmos/xmm53_release/

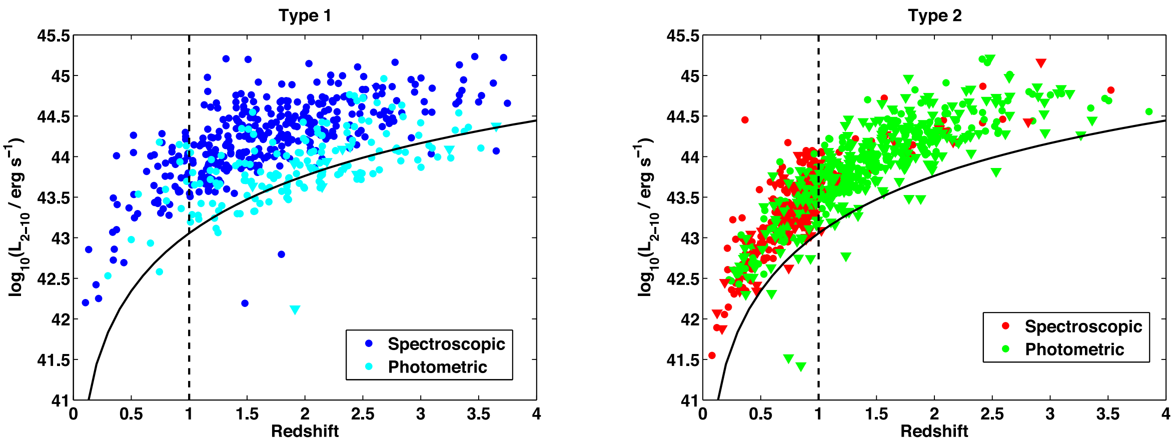

Figure 2. Redshift versus observed hard (2–10 keV) band luminosity for type 1 AGN (left) and type 2 AGN (right). Both spectroscopic and photometric AGN are shown. The circles mark actual detections whereas the downward triangles represent upper limits in the case of the type 2 AGN and hard-band luminosities estimated from the soft-band flux in the case of the type 1 AGN. The solid lines denote the flux limit applied to the data to generate homogenous populations of the two populations for our stacking analysis. The vertical dashed lines correspond to $z > 1$ which is the redshift cut applied before stacking such that the 850-µm flux is invariant with dust luminosity as a function of redshift.

In the majority of the analysis presented in this paper, we consider the average stacked submillimeter fluxes of AGN as a function of various properties. For these stacking studies, we construct flux-limited populations of AGN restricted to sources with $S > 2.5 \times 10^{-15}$ erg s^{-1} cm^{-2} in the hard (2–10 keV) band (Lusso et al. 2011). As previously mentioned, type 1 AGN that are detected in the soft band but not in the hard band, have had their hard band fluxes estimated from the soft X-ray flux using a $\Gamma = 1.8$ power-law spectral energy distribution (SED). Type 2 AGN that are detected in the soft band only have been discarded for the majority of the stacking analysis due to their essentially unknown dust columns and therefore intrinsic luminosities. These soft-band-detected type 2 AGN are however included when searching for AGN that are individually detected at 850 µm in Section 3. The hard-band X-ray flux limit is illustrated in Fig. 2 and corresponds to $L_X \gtrsim 10^{43}$ erg s^{-1} at $z > 1$, where the X-ray luminosity should be completely dominated by AGN activity. We also restrict ourselves to only those AGN at $z > 1$ for all the stacking analysis. At $z > 1$, the 850-µm flux is essentially invariant with redshift for a given dust luminosity and therefore SFR, allowing us to average the submillimeter fluxes of AGN over relatively wide redshift bins in order to improve the statistical significance of our results. The 850-µm data does not however trace the peak of the dust SED at these redshifts and there could potentially be biases in how effectively this submillimeter flux is tracing star formation due to variations in the template SEDs over this rest-frame wavelength range. In Section 4.1, we will therefore explicitly check the dependence of 850-µm flux on SFRs.

Finally, there is a concern that the 850-µm flux could be contaminated by synchrotron emission for populations of radio-loud AGN. The fraction of radio-loud AGN in X-ray-selected AGN samples is expected to be small ($\lesssim$5 per cent for type 1 AGN from Hao et al. 2014). Nevertheless, we match the X-ray AGN sample to the VLA radio catalogue (Schinnerer et al. 2010) and remove all sources with $S_{1.4\mathrm{GHz}} > 0.5$ mJy. This removes 10 type 1 and 7 type 2 AGN at $z > 1$ from the sample, which represents ~2 per cent of both the type 1 and type 2 samples.[2] The radio flux limit imposed corresponds to a synchrotron 850-µm flux of <0.01 mJy assuming a synchrotron spectral index of 0.7. Therefore, we can be confident that the 850-µm stacks that we study are completely dominated by thermal dust emission. Our final $z > 1$ AGN sample used in the stacking analysis, totals 699 AGN. These are comprised of 428 type 1 AGN (314 spectroscopic, 114 photometric) and 271 type 2 AGN (46 spectroscopic, 225 photometric).

Bongiorno et al. (2012) have used SED fits to the multiwavelength COSMOS photometry, in order to estimate stellar masses, SFRs and other host galaxy parameters for these type 1 and type 2 AGN. Both galaxy and AGN components are fit allowing us to study the dependence of 850-µm flux densities on a wide range of AGN and host galaxy properties. These SED fits incorporate photometry at optical, near-infrared as well as mid-infrared wavelengths. Around 80 per cent of the sources are detected in the *Spitzer* MIPS 24-µm band. In addition, several of the AGN are also detected in the MIPS 70-µm band as well as in the *Herschel*-PACS 100-µm and 160-µm bands (Bongiorno et al. 2012). All of this multiwavelength photometry is used in the SED fitting and both pure AGN and pure galaxy templates are allowed in the fits. The galaxy templates constitute a set of Bruzual & Charlot (2003) stellar population synthesis models with a Chabrier (2003) initial mass function and assuming exponentially declining star formation histories with varying amounts of dust reddening. The AGN template is the mean quasar SED from Richards et al. (2006), again with varying amounts of reddening. This choice of AGN template is appropriate for the luminous *XMM*-COSMOS AGN investigated in this work. Bongiorno et al. (2012) have already discussed the accuracy of the stellar mass estimates for both the type 1 and type 2 AGN samples and when considering the properties of the AGN as a function of stellar mass, we only consider those AGN that have robust stellar masses as specified by the *flags* parameter. As expected, >99.5 per cent of the type 2 AGN have robust stellar mass estimates.

2.2.1 *Limitations of the X-ray AGN catalogue*

In this analysis, we consider the submillimeter properties of a hard X-ray flux-limited catalogue of AGN. However, before proceeding it is important to highlight the selection biases and incompletenesses of an AGN catalogue selected in this way. Donley et al. (2012) have

---

[2] Including these radio-detected AGN in the 850-µm stacking does not change the average 850-µm flux derived for our sample in Section 4 to within 0.1 mJy.

Table 1. Summary of X-ray AGN with potential 850-µm bright identifications in the COSMOS field. The corrected Poisson probability of a chance association is quoted as calculated from the soft X-ray flux and the hard X-ray flux, respectively. Sources with photometric redshifts are marked with a *pz*. Sources with hard X-ray luminosities marked with an asterisk are type 1 AGN that are only detected in the soft band and where the hard band luminosity has been calculated assuming $\Gamma = 1.8$.

XID	RA	Dec	Redshift	$\log_{10}(L_{2-10})$ (erg s^{-1})	Separation (arcsec)	$S_{0.5-2\mathrm{keV}}$ (erg s^{-1} cm^{-2})	$p_{0.5-2\mathrm{keV}}$	$S_{2-10\mathrm{keV}}$ (erg s^{-1} cm^{-2})	$p_{2-10\mathrm{keV}}$	S_{850} (mJy)
13	150.009 24	2.275 5119	0.850	43.95	3.42	2.11e-14	0.0006	2.9e-14	0.0009	4.5 ± 1.1
18	150.133 04	2.303 2850	1.598	44.92	5.92	1.80e-14	0.002	6.04e-14	0.0009	4.4 ± 1.2
139^{pz}	150.041 84	2.629 4839	0.739	43.69	3.30	9.52e-15	0.001	2.22e-14	0.001	7.4 ± 1.7
160	150.158 39	2.139 6031	1.825	44.28	1.48	2.39e-15	0.001	1.02e-14	0.0008	8.1 ± 1.2
246^{pz}	150.051 00	2.493 8550	2.342	44.56	3.65	8.81e-16	0.008	1.09e-14	0.003	6.4 ± 1.7
250	150.064 55	2.329 0511	2.446	44.14*	3.04	2.41e-15	0.004	<3.78e-15	–	4.0 ± 1.1
270^{pz}	150.106 12	2.014 4781	1.883	<44.13	1.83	1.17e-15	0.003	<6.64e-15	–	9.8 ± 1.7
278^{pz}	150.093 08	2.101 4100	2.269	<44.46	2.61	1.46e-15	0.004	<9.39e-15	–	5.0 ± 1.4
353	150.084 38	2.290 4881	1.112	43.70	2.04	2.34e-15	0.002	8.57e-15	0.002	4.7 ± 1.0
402^{pz}	150.252 26	2.261 9131	1.078	43.57	2.86	2.22e-15	0.003	6.82e-15	0.003	5.7 ± 1.5
415^{pz}	149.969 81	2.183 4869	1.558	43.33*	2.90	1.04e-15	0.005	<8.31e-15	–	5.5 ± 1.4
469^{pz}	150.096 85	2.021 5000	3.362	<44.45	2.22	1.08e-15	0.004	<3.73e-15	–	6.6 ± 1.7
10675	150.192 62	2.219 8489	3.090	43.92*	0.28	8.45e-16	0.0001	<1.73e-15	–	5.7 ± 1.2
10809^{pz}	150.207 58	2.381 6111	1.288	<44.15	1.79	1.12e-15	0.003	<1.7e-14	–	6.5 ± 1.5
30182^{pz}	150.125 41	2.697 8931	0.742	43.23	6.00	6.26e-15	0.005	7.52e-15	0.009	6.9 ± 1.7
53922	150.094 54	2.702 9131	0.850	43.38	1.81	2.25e-15	0.002	7.74e-15	0.001	8.6 ± 1.8
54440^{pz}	150.063 08	1.944 6778	1.947	43.91	4.39	1.13e-15	0.009	<3.74e-15	–	7.7 ± 1.7
60070^{pz}	150.227 19	2.232 4781	2.066	<44.01	1.93	7.33e-16	0.003	<4.11e-15	–	5.8 ± 1.4
60490^{pz}	150.105 44	2.185 2681	1.089	43.42	5.33	<7.57e-16	–	4.76e-15	0.011	6.9 ± 1.1

used a mid-infrared IRAC selection for AGN candidates in the COSMOS field demonstrating that only ∼38 per cent of these AGN candidates have X-ray counterparts due to the relatively shallow flux limit of the *XMM*-COSMOS hard X-ray data. Hence, we may potentially be missing a significant population of heavily obscured to mildly Compton thick AGN in this analysis. Recently, Lacy et al. (2015) have also used mid-infrared-selected AGN samples to demonstrate that X-ray surveys begin to become incomplete at $z \gtrsim 1.6$ where a deficit in the X-ray luminosity function is seen relative to the mid-infrared luminosity function even in the highest luminosity bins. We refer readers to these papers for a detailed consideration of the incompleteness in hard X-ray-selected samples of AGN.

2.3 Non-AGN Galaxy catalogue

Finally, as a control sample to compare the AGN properties to, we also utilize a galaxy sample from the UltraVISTA survey Data Release 1 (McCracken et al. 2012) over the same region. We work with the *K*-band flux-limited sample from Muzzin et al. (2013), which essentially represents a mass-limited sample of galaxies. Corresponding photometric redshifts, stellar masses and other SED-fitting parameters are also taken from Muzzin et al. (2013). An advantage of using a galaxy catalogue that is selected in the redder *K*-band, is that these catalogues are potentially more sensitive to dusty galaxies that would be detected at 850 µm compared to galaxy catalogues constructed using data at optical wavelengths. We note that several previous studies that we compare our results to in this paper, have used non-AGN galaxy samples selected using flux-limited surveys at bluer (optical) wavelengths.

3 850-µm DETECTED AGN

We begin by looking for AGN that are detected at $>3.5\sigma$ in the SCUBA-2 CLS 850-µm catalogues. As stated above, only regions with $\sigma_{850} < 2$ mJy were used in the construction of the 850-µm catalogue, which therefore does not cover the entire field. A matching radius of 7.5 arcsec is used to associate 850-µm catalogued sources with our AGN sample. The AGN positions in all cases correspond to the optical positions from Brusa et al. (2010), which have much smaller uncertainties than the *XMM–Newton* X-ray positions. Given the errors on the optical positions are likely to be negligible, we follow Ivison et al. (2007) and assume that for a signal-to-noise ratio (SNR) of 3.5, the positional uncertainty, $\sigma_{\mathrm{pos}} = 0.6\times\mathrm{FWHM/SNR}$. For an FWHM of 14.5 arcsec at 850 µm, σ_{pos} is therefore 2.5 arcsec and the 7.5 arcsec matching radius corresponds to $3\sigma_{\mathrm{pos}}$ and is therefore expected to encompass >99.7 per cent of true counterparts.

There are a total of 19 850-µm sources that lie within 7.5 arcsec of an X-ray AGN and there are no instances of multiple submillimeter sources matched to the same X-ray AGN. All 19 matches are presented in Table 1 and we estimate the corrected Poisson probability, p_{corr} of these being chance associations based on the background density of all X-ray AGN that have fluxes brighter than the target being considered. Specifically,

$$p_{\mathrm{raw}} = 1 - \exp\left(\pi r^2 N(>S)\right)$$
$$p_{\mathrm{det}} = 1 - \exp\left(\pi r_{\mathrm{max}}^2 N(>S_{\mathrm{lim}})\right)$$
$$p_{\mathrm{corr}} = 1 - \exp\left(p_{\mathrm{raw}}\left(1 + \ln\left(\frac{p_{\mathrm{raw}}}{p_{\mathrm{det}}}\right)\right)\right), \qquad (1)$$

where r is the separation between the submillimeter source and the X-ray AGN, r_{max} is the maximum search radius and $N(>S)$ and $N(>S_{\mathrm{lim}})$ represent the background surface density of AGN brighter than the source being considered and brighter than the flux limit of the survey, respectively. We estimate $N(>S)$ using the source counts in the soft and hard X-ray bands from Cappelluti et al. (2009) and assume $S_{\mathrm{lim}} = 5\mathrm{e}{-16}$ erg s^{-1} cm^{-2} and 2.5e-15 erg s^{-1} cm^{-2} in the 0.5–2 and 2–10 keV bands, respectively. Given the low surface density of X-ray AGN and submillimeter sources, all 19 matches have very small probabilities ($\lesssim$1 per cent) of being chance associations (see

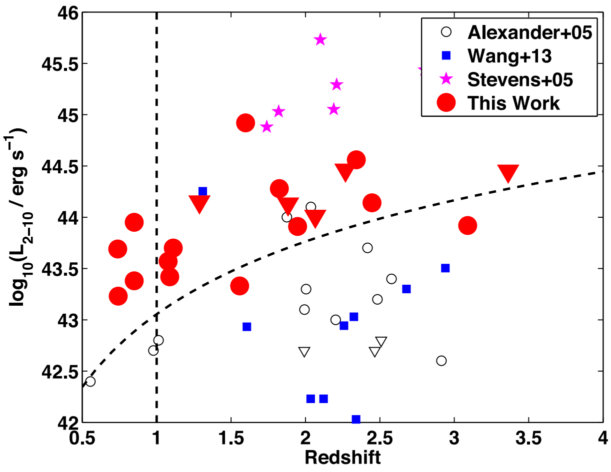

Figure 3. Redshift versus observed hard X-ray (2–10 keV) luminosity for the X-ray AGN that are individually detected at submillimeter wavelengths in this work and compared to individually detected submillimeter bright X-ray AGN from Alexander et al. (2005) and Wang et al. (2013) and submillimeter detected quasars from Stevens et al. (2005). Downward triangles denote upper limits. The hard X-ray flux limit and $z > 1$ redshift limit applied prior to our stacking analysis, are denoted by the dashed lines. Both Alexander et al. (2005) and Wang et al. (2013) probe fainter X-ray luminosities compared to our work, while the X-ray AGN from Stevens et al. (2005) that were individually followed up, probe very high X-ray luminosities. Our study is useful in bridging the gap between these different data sets.

Table 1). The 19 sources are comprised of six spectroscopically confirmed broad-line AGN, one spectroscopically confirmed narrow-line AGN, three AGN with photometric redshifts that are best fit by type 1 AGN templates and nine AGN with photometric redshifts that are best fit by type 2 AGN or galaxy templates. Thus, out of a sample of 360 850-μm bright sources, we find that ∼5 per cent are associated with X-ray luminous AGN. The *XMM*-COSMOS data used in this work corresponds to relatively bright AGN X-ray flux limits as can be seen in Fig. 2. Wang et al. (2013) identify the X-ray counterparts to Atacama Large Millimeter Array-detected submillimeter bright galaxies in the Extended Chandra Deep Field South (E-CDFS). *Chandra* observations are used to go down to X-ray luminosities of $\sim 7 \times 10^{42}$ erg s^{-1} and the authors find a larger AGN fraction of ∼17 per cent among the submillimeter galaxies. However, as can be seen in their fig. 10, this AGN fraction decreases as a function of increasing X-ray luminosity. Down to similar X-ray luminosities as Wang et al. (2013), Symeonidis et al. (2014) find an AGN fraction of 18 per cent among infrared luminous galaxies in the CDF-N and CDF-S fields at $z < 1.5$. Alexander et al. (2005) have used ultradeep X-ray observations in the CDF-N to study the AGN fraction in $S_{850} \gtrsim 4$ mJy sub-mm bright galaxies at $z > 1$, finding that the majority host AGN activity. However, the X-ray data from *Chandra* used in that work, is an order of magnitude fainter than our *XMM*-COSMOS sample. In Fig. 3, we plot the redshift versus hard (2–10 keV) X-ray luminosity for the submillimeter-detected AGN in this work as well as Alexander et al. (2005) and Wang et al. (2013). We also show here the submillimeter-detected X-ray absorbed quasars from Stevens et al. (2005), which were selected using X-ray surveys with *ROSAT*, *XMM–Newton* and *Chandra* and followed up at submillimeter wavelengths using SCUBA. The Wang et al. (2013) observed 0.5–8 keV luminosities have been converted to 2–10 keV luminosities assuming the intrinsic photon indices derived for each object in that paper whereas conversions from 0.5–2 keV fluxes in Stevens et al. (2005) assume $\Gamma = 1.8$. Our work can immediately be place in the context of these previous studies. While both Alexander et al. (2005) and Wang et al. (2013) probe significantly fainter in terms of X-ray luminosity, our sample fills in the luminosity gap between these studies and the individual follow-up observations of X-ray bright quasars by Stevens et al. (2005). The X-ray brightest sub-mm AGN in our sample is brighter than any of the X-ray AGN detected in the sub-mm by Alexander et al. (2005) and Wang et al. (2013). It corresponds to XID18 and is an extremely red AGN with evidence for outflowing gas with velocities of ∼300 km s^{-1} (Brusa et al. 2015). This class of objects will be discussed later in Section 4.4.

Herschel fluxes for all 850-μm detected sources are extracted from the catalogues of Swinbank et al. (2014) by matching the optical positions of the AGN in our catalogue to the 24-μm positions in the *Herschel* catalogues, using a matching radius of 3 arcsec. The *Herschel* catalogues have already been corrected for blending using the 24-μm positional priors (Swinbank et al. 2014). These fluxes are presented in Appendix B together with other derived properties for these submillimeter bright X-ray AGN. As the *Herschel* fluxes have been extracted by Swinbank et al. (2014) using the 24-μm positional priors, all 24-μm detected sources have measured *Herschel* fluxes whereas sources not detected at 24 μm are not in the *Herschel* catalogues.

4 AVERAGE 850-μm EMISSION FROM STACKED SUB-SAMPLES

The majority of the X-ray AGN are not individually detected in the 850-μm catalogue, which goes down to a 3.5σ flux limit of ∼3.5 mJy in the highest sensitivity regions. To understand the average submillimeter properties of the AGN, we therefore have to study stacked 850-μm maps. We begin by constructing an inverse variance weighted stacked image at 850 μm for all 699 $z > 1$ AGN (428 type 1 and 271 type 2) that will be used from hereon in our stacking analysis. Specifically,

$$S_{ij} = \frac{\Sigma_{k=1}^{N} P_{ij} \times f_{ij}^{k}/(\sigma_{ij}^{k} \times \sigma_{ij}^{k})}{\Sigma_{k=1}^{N} P_{i,j}/(\sigma_{ij}^{k} \times \sigma_{ij}^{k})}, \tag{2}$$

where S_{ij} represents the stacked 850-μm image, P_{ij} is the point response function of SCUBA-2 at 850 μm generated by stacking all $>10\sigma$ sources in the map, f_{ij} are the 40×40 pixel (80 arcsec × 80 arcsec) flux images of each of the N sources going into the stacks and σ_{ij} are the corresponding rms images. Stacked images generated in this way can be seen in Fig. 4 for both the AGN sample and a set of random points in the map, where any random points within 7.5 arcsec of a catalogued 850-μm source, have been removed. Fig. 4 clearly demonstrates the presence of a statistically significant 850-μm signal from the $z > 1$ X-ray AGN relative to the random points. The typical rms noise in the maps is well above the confusion limit. As stated in Section 2.1, the noise is non-uniform over the full 2 deg^2 map. Out of the 699 $z > 1$ sources being stacked, 80 per cent lie in regions with rms noise <3.5 mJy. From the 850-μm source counts presented in Casey et al. (2013), we estimate that the integral source count at this rms noise level is only ∼630 deg^{-2}. Assuming a beam FWHM of 14.5 arcsec for SCUBA-2 at 850 μm, the beam density is ∼78 000 deg^{-2}. Hence, only 1 in 120 beams is expected to be affected by confusion at this rms noise. In the lowest rms regions in our map (σ = 1 mJy), the integral source counts reach ∼3000 deg^{-2} and 1 in 25 beams is affected by confusion, which is still a small effect.

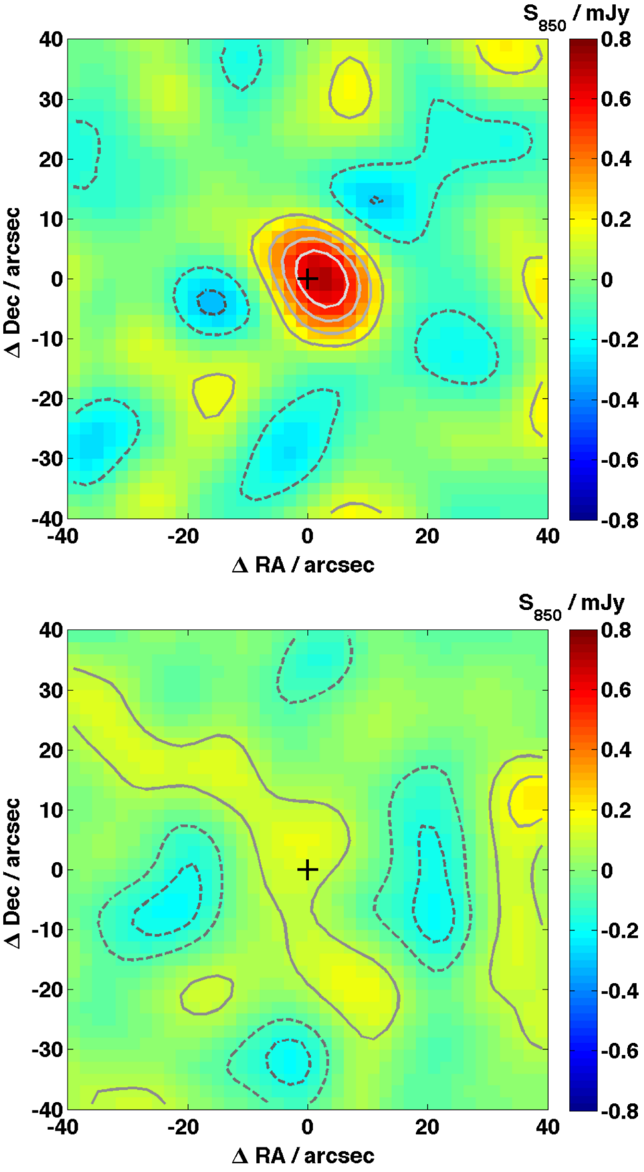

Figure 4. 80 arcsec×80 arcsec weighted, stacked 850-μm images centred on the positions of the 699 $z > 1$ X-ray AGN in our flux limited sample (top) and centred on exactly the same number of random points (bottom). The AGN stack includes 428 type 1 AGN and 271 type 2 AGN. The colour scaling is the same in both images. The contours are at 1σ–5σ and the solid contours correspond to positive fluxes whereas the dashed contours correspond to negative fluxes. We clearly observe a statistically significant 850-μm detection from the AGN relative to the random points.

Before investigating the dependence of the 850-μm emission on the AGN properties, we first describe our methodology for calculating the stacked 850-μm fluxes. Throughout this analysis, the stacked 850-μm flux is measured as the median or mean value of the central pixel in 100 bootstrapped inverse variance weighted stacked images (see equation 2). We have already checked in Section 2.1 that the astrometry of the SCUBA-2 map is accurate to within a pixel so this central pixel flux provides the most conservative and unbiased estimate of the average flux. The central pixel flux is measured to be 0.71 ± 0.08 mJy for all 699 AGN. The median redshift of the sample is $z = 1.66$ and the median hard X-ray luminosity is $\log_{10}(L_{2\text{–}10}) = 44.2$. We emphasize that these X-ray luminosities correspond to the most luminous AGN in the 'quasar' regime. For comparison, the average 870-μm flux of the Lutz et al. (2010) AGN is 0.49 ± 0.04mJy. The Lutz et al. (2010) sample has both a lower median redshift ($z = 1.17$) and a lower median hard X-ray luminosity – $\log_{10}(L_{2\text{–}10}) = 43.6$ calculated from the median hard X-ray flux in that paper and using our assumed value of $\Gamma = 1.8$ as described in Section 2.2. Given these differences in the median properties of the two samples as well as the correction from 870 to 850 μm for a typical single temperature greybody SED and the statistical errors in both measurements, our results are broadly consistent with those of Lutz et al. (2010). Excluding the individually detected 850-μm X-ray AGN described in Section 3 from the stacks, we find that the average flux falls to 0.60 ± 0.07 mJy, which is still a $>8\sigma$ detection.

We have checked that the median and mean stacked fluxes are very similar in both cases. The error on the flux is calculated using 100 bootstrap samples. We also calculate stacked fluxes using the publicly available code SIMSTACK (Viero et al. 2013). The code is designed to correctly account for clustering of sources within the scale of the SCUBA-2 beam which is assumed to be 14.5 arcsec. The method essentially involves performing a regression of the true flux map with a 'hits' map, where the 'hits' map is created by counting the number of sources to be stacked that contribute to each pixel in the map. We stack the 699 flux-limited $z > 1$ AGN with the $z < 1$ AGN. If the photometric redshifts are accurate, there should be no clustering between the high and low redshift AGN populations. The stacked 850-μm flux for the 699 $z > 1$ AGN is 0.82 ± 0.02 mJy from SIMSTACK which is slightly higher than our central pixel flux measurement. The higher SIMSTACK flux is likely due to the fact that the peak 850-μm emission in Fig. 4 is offset from the central pixel. The SIMSTACK errors reflect the regression errors and do not account for any errors due to sample variance. Our bootstrap errors are therefore more conservative. The SIMSTACK results demonstrate that the central pixel flux represents a conservative estimate and is not biased up due to clustering. For the rest of the analysis, we therefore use the central pixel flux to measure the average submillimeter emission for all the sub-samples we construct. As a final check, given that some regions of the 850-μm wide S2CLS COSMOS maps are significantly noisier than others (Section 2.1), we also restrict our stacks only to the regions with σ_{850} <2mJy to mitigate against the effects of flux boosting. There are 341 $z > 1$ X-ray AGN in our flux-limited sample in these high-sensitivity regions and the mean flux is $S_{850} = 0.69 \pm 0.10$ mJy, consistent with the results derived using the entire 850-μm wide map. We will therefore proceed with using the 850-μm data over the full COSMOS wide area for all the stacking analysis that follows.

Before continuing, it is important to highlight the assumptions inherent in our work. Throughout this paper, we assume that the 850-μm flux is tracing the total amount of cool dust emission in the AGN host galaxies and that this cool dust is primarily heated by star formation and has a negligible contribution from the AGN. Given that the 850-μm flux is invariant with redshift at $z > 1$, we can average these fluxes over relatively broad redshift bins without bias. Note that this is not the case for *Herschel* fluxes for example, which trace the peak of the dust SED at $z \sim 1$–3, and are expected to be varying more strongly with redshift. As we do not have large enough AGN samples to be able to split our AGN into narrow redshift bins, we restrict our analysis to the 850-μm properties only rather than constructing full SEDs from the *Herschel* and 850-μm data. The 850-μm emission can also only be used as a proxy for the SFR provided the dust temperature is not varying significantly between AGN sub-samples, and also assuming that the dust heating at these wavelengths is dominated by recent star formation rather than being dominated by cold dust heated by old stars and the interstellar medium (e.g. Bourne et al. 2013). We therefore begin by testing how the 850-µm flux varies with SFR.

4.1 Star formation rate

Bongiorno et al. (2012) have estimated the SFRs for the COSMOS AGN using SED-fitting to the available multiwavelength photometry (Brusa et al. 2010) – $\mathrm{SFR}_{\mathrm{SED}}$ hereafter. These can be used to check the dependence of the 850-µm flux density on SFR. As described in Section 2.2, the SED based SFRs include photometry in the *Spitzer* IRAC as well as MIPS 24-µm bands in most cases. In some cases, the SED fits also include longer wavelength photometry at MIPS 70 µm as well as at *Herschel* 100 and 160 µm. We select only the type 2 $z > 1$ AGN with robust SFR estimates as specified by the *flags* parameters in Bongiorno et al. (2012). We note that soft X-ray-detected type 2 AGN that are not detected in the hard band are also included in this analysis to improve the statistics. Here, we are primarily concerned with checking whether the 850-µm fluxes correlate with other independently derived SFR constraints and knowledge of the true dust columns and therefore intrinsic X-ray luminosities of the AGN is not relevant. In luminous, unobscured type 1 AGN, the big blue bump typically seen in quasar spectra may mimic the UV bump from massive stars so SFRs based on SED fitting are no longer reliable. Hence, type 1 AGN are not considered in this test.

We split the type 2 AGN into two $\mathrm{SFR}_{\mathrm{SED}}$ bins at $\mathrm{SFR} > 10\,\mathrm{M}_{\odot}\,\mathrm{yr}^{-1}$ and $\mathrm{SFR} < 10\,\mathrm{M}_{\odot}\,\mathrm{yr}^{-1}$. The median redshifts are $z = 1.36$ and 1.77 for the low and high $\mathrm{SFR}_{\mathrm{SED}}$ sub-samples, respectively. The median SFRs are 1.5 and 33 $\mathrm{M}_{\odot}\,\mathrm{yr}^{-1}$ while the mean SFRs are 1.1 and 46 $\mathrm{M}_{\odot}\,\mathrm{yr}^{-1}$ in the two bins. The average 850-µm fluxes for these sub-samples are 0.3 ± 0.1 and 1.0 ± 0.2 mJy, respectively and are therefore clearly higher in the higher SFR bin. The excess 850-µm flux in the high SFR bin is significant at the $\sim 3\sigma$ level. Several previous studies have instead used the 250-µm fluxes as a proxy for SFR. We therefore also calculate average *Herschel* 250-µm fluxes for the type 2 AGN in these two SFR bins although we caution that the bins encompass AGN over a relatively broad range of redshifts, which could be adding scatter to the 250-µm fluxes. The 250-µm fluxes are calculated by injecting the AGN in each SFR bin in turn into the *Herschel* SPIRE 250-µm map from Swinbank et al. (2014), which has had all 24-µm-detected sources removed. The maps are then stacked at the AGN position and the average flux is once again measured as the value at the central pixel. Note that we have also checked the astrometry of the 250-µm map in Section 2.1. The 250-µm fluxes in these two SFR bins are 2.0 ± 0.3 mJy and 5.3 ± 0.6 mJy, respectively. In order to check whether the 250-µm and 850-µm stacks are consistent with each other, we fit a single temperature greybody with $\beta = 2.0$ to these data points in the two SFR bins. The dust temperatures are 24 ± 6 and 27 ± 5 K, respectively, consistent with a single temperature in both SFR bins. From the integral under the greybody, we can then calculate the far-infrared luminosity (between 60 and 300 µm to eliminate any contributions from the AGN) and average SFR for each stack. These are $\log_{10}(L_{\mathrm{FIR}}/\mathrm{L}_{\odot}) = 10.9 \pm 0.3$ corresponding to $\mathrm{SFR} = 12\pm^{11}_{6}\,\mathrm{M}_{\odot}\,\mathrm{yr}^{-1}$ for the low SFR stack and $\log_{10}(L_{\mathrm{FIR}}/\mathrm{L}_{\odot}) = 11.5 \pm 0.2$ corresponding to $\mathrm{SFR} = 60\pm^{30}_{20}\,\mathrm{M}_{\odot}\,\mathrm{yr}^{-1}$ for the high SFR stack. In both cases, the SFRs derived from the *Herschel* and 850-µm data are higher than the mean SFRs from Bongiorno et al. (2012) although the error bars and scatter in both average SFR measurements are large. In Appendix B, where we have shown best-fitting far-infrared SEDs for our X-ray AGN that are individually detected at 850 µm, we also show that the far-infrared luminosity and SFR as measured from these best-fitting SEDs, correlates well with both the 250- and 850-µm fluxes (Fig. B2). In Appendix B, the dust mass from full SED fitting has also been plotted against both the 250- and 850-µm fluxes and in general shows a weaker correlation with the infrared and sub-mm flux densities compared to the far-infrared luminosity. We will therefore proceed by assuming that the stacked 850-µm flux in our $z > 1$ AGN is giving us a direct estimate of the average SFR, with the caveat that for galaxies with low levels of star formation, there may also be a contribution to the dust heating at 850 µm from old stars and the interstellar medium.

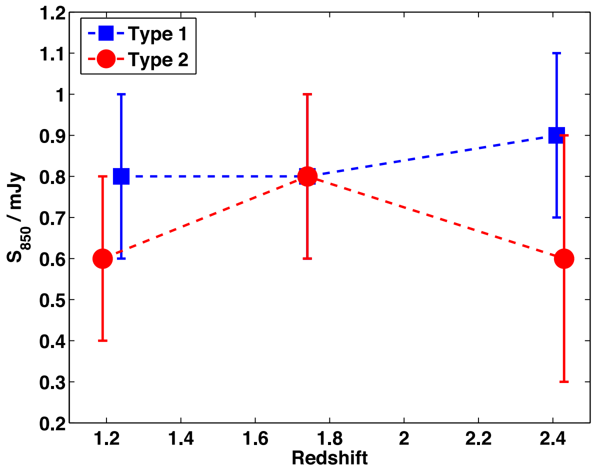

Figure 5. Average 850-µm flux versus redshift for both type 1 and type 2 AGN.

4.2 Redshift

The size of our current sample necessitates stacking over relatively broad redshift bins. Evolutionary effects could therefore influence any derived results and introduce differences in stacked 850-µm fluxes between different sub-samples. Before looking for trends with other AGN properties, we therefore first consider the redshift evolution of the 850-µm fluxes over the full redshift range considered in our stacked analyses. In order to do this, we split the $z > 1$ type 1 and type 2 AGN into three redshift bins and consider their stacked 850-µm fluxes. The results are illustrated in Fig. 5. Both the type 1 and type 2 AGN submillimeter fluxes show little evolution with redshift over the redshift range probed in this work. In all three redshift bins, the type 1 and type 2 AGN 850-µm fluxes are consistent with each other given the error bars. When considering trends in AGN submillimeter fluxes with luminosity, obscuration and AGN activity in the following sections, we will therefore assume that the 850-µm fluxes do not evolve with redshift over the redshift range considered.

4.3 X-ray luminosity

We now explore trends in these 850-µm fluxes with the hard X-ray luminosity, which can be used as a proxy for the energy emitted by the central accreting power source. Several recent studies have found a reasonably flat relationship between AGN luminosity and SFR (e.g. Harrison et al. 2012; Rosario et al. 2012; Azadi et al. 2015; Stanley et al. 2015). At modest X-ray luminosities where large samples of X-ray AGN with far-infrared and submillimeter data now exist, these results are now robust. However, the situation

Table 2. Stacked 850-µm fluxes for the type 1 and type 2 AGN in three bins in hard X-ray luminosity. Detections above 3σ are shown in bold and the number of sources in each bin is given in brackets.

	Type 1 AGN	Type 2 AGN
$43.5<\log_{10}(L_{2-10}/\,\mathrm{erg\ s^{-1}})<44.0$	0.7 ± 0.3 ($N = 102$)	0.5 ± 0.2 ($N = 114$)
$44.0<\log_{10}(L_{2-10}/\,\mathrm{erg\ s^{-1}})<44.4$	**1.0 ± 0.2** ($N = 168$)	**0.6 ± 0.2** ($N = 94$)
$\log_{10}(L_{2-10}/\,\mathrm{erg\ s^{-1}})>44.4$	**0.7 ± 0.2** ($N = 146$)	**1.3 ± 0.3** ($N = 50$)

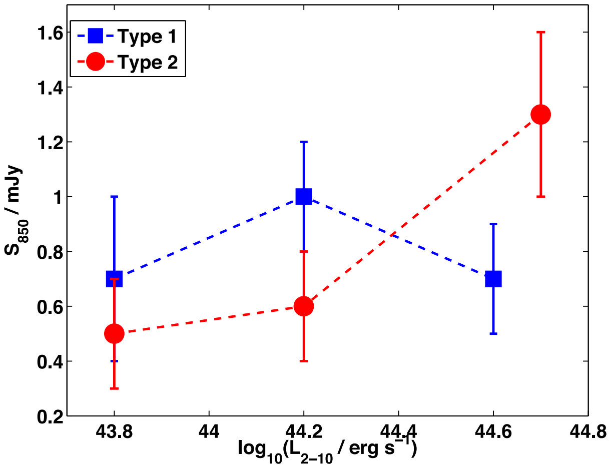

Figure 6. Average 850-µm flux versus hard X-ray luminosity for both type 1 and type 2 AGN.

is less clear at very high X-ray luminosities. While Page et al. (2012) have suggested that the far-infrared fluxes and therefore SFRs of AGN with high X-ray luminosities, are suppressed relative to AGN of lower luminosity, Lutz et al. (2010) and Rosario et al. (2012) instead find an increase in SFR at high X-ray luminosities, with the results being more pronounced for low redshift AGN in Rosario et al. (2012). The results from recent hydrodynamical simulations suggest that there is a large scatter in the L_X–SFR relation over the dynamic range probed by current surveys (Sijacki et al. 2015), which may explain some of the discrepancies between previous studies.

The SCUBA-2 photometry presented in this paper now allows an independent investigation of the relation between star formation and AGN luminosity with the advantage that the submillimeter flux is less contaminated by AGN emission than the *Herschel* fluxes in the case of the most luminous quasars. As illustrated in Fig. 2, at $z > 1$, the COSMOS field is only complete at relatively high X-ray luminosities. We select type 1 and type 2 AGN in three X-ray luminosity bins – $43.5< \log_{10}(L_{2-10}) < 44$, $44.0< \log_{10}(L_{2-10}) < 44.4$ and $\log_{10}(L_{2-10}) > 44.4$. The AGN that are individually detected at 850 µm (see Section 3) are also included in the stack. There are only 7 X-ray AGN out of the 19 that satisfy both the hard X-ray flux limit and the $z > 1$ redshift cut and we have checked that inclusion of these AGN does not change the stacked fluxes quoted within the error bars. Note that the lowest X-ray luminosity bin is incomplete at $z \gtrsim 2$ so the results here should be interpreted with caution. The average 850-µm fluxes are presented in Table 2 and illustrated in Fig. 6. While the type 1 submillimeter flux appears to be fairly independent of X-ray luminosity, there is some evidence that the most X-ray luminous type 2 AGN have higher submillimeter fluxes. The type 2 AGN at $\log_{10}(L_{2-10}) > 44.4$ have 850-µm fluxes that are $\sim 2\sigma$ higher than in the previous X-ray bin although the numbers of type 2 AGN at such high X-ray luminosities are small so the results could be affected by small number statistics.

In the highest X-ray luminosity bin, the AGN are expected to have a relatively narrow Eddington ratio distribution based on the models of Aird et al. (2013). These AGN therefore likely correspond to high-mass black holes hosted in massive galaxies. If AGN were preferentially found in star-forming galaxies on the main sequence, these massive galaxies would be expected to have higher SFRs. The high X-ray luminosity bins may therefore be dominated by a larger fraction of quiescent hosts for the type 1 AGN, which would naturally explain the lower 850-µm fluxes. X-ray luminous type 1 AGN could also represent a skewed population of highly accreting black holes seen during a brief phase of black hole growth. As such, their host galaxies may be undermassive relative to their black hole masses, and this could once again explain the lower dust luminosities and therefore SFRs in these sources.

The type 2 AGN show a more marked increase in average submillimeter flux with X-ray luminosity with the most X-ray luminous AGN having higher SFRs. As can be seen in Fig. 2, for a flux-limited sample, the median redshift increases with increasing X-ray luminosity. However, we have shown in Section 4.2 that the 850-µm flux does not evolve significantly with redshift in the type 2 AGN population. Therefore, the trend observed in Fig. 6 is unlikely to be driven by redshift. Evidence of higher SFRs in more X-ray luminous AGN was also found by Lutz et al. (2010) who argue for two modes of star formation in the population – secular and merger driven. The most X-ray luminous type 2 AGN could therefore represent a transition to a merger-driven scenario where star formation and black hole accretion are more tightly coupled. Fig. 6 also suggests that there may be systematic differences in the host galaxy properties of the most X-ray luminous type 1 and type 2 AGN with the luminous type 2 AGN occupying more highly star-forming galaxies. Alternatively, it is possible that the type 2 AGN have higher 850-µm fluxes simply as a result of a higher dust mass relative to their type 1 counterparts of comparable luminosity.

Overall, it is difficult to establish a direct causal connection between AGN activity and star formation when studying average properties of AGN host galaxies over a wide range in luminosity, redshift and host galaxy type. The situation is further complicated by the fact that the time-scales for star formation and AGN activity are very different so AGN variability can wipe out any underlying correlations (Gabor & Bournaud 2013; Hickox et al. 2014). Indeed, the AGN that are individually detected at $>3.5\sigma$ at 850 µm (Table 1) have a range of hard X-ray luminosities and would populate all three X-ray luminosity bins considered in this analysis. However, at least in the type 2 AGN population there appears to be evidence for a transition to more highly star-forming hosts and/or higher dust mass at the highest X-ray luminosities.

Table 3. Summary of stacked 850-µm fluxes for sub-samples of AGN selected according to various obscuration parameters. Detections above 3σ are shown in bold.

Parameter investigated	Sample	N	z	$\log_{10}(L_{2-10}/\mathrm{erg\ s^{-1}})$	S_{850} (mJy)
Spectroscopic/Photometric classification	Type 1	428	1.78	44.2	**0.8 ± 0.1**
	Type 2	271	1.45	44.0	**0.6 ± 0.1**
Hardness ratio	Type 1 and 2 $HR > -0.2$	129	1.60	44.2	0.7 ± 0.3
	Type 1 and 2 $HR < -0.2$	346	1.61	44.3	**0.7 ± 0.1**
Optical/Infrared colour	Type 1 and 2, $(r-4.5) > 6.1$ (Vega)	303	1.56	44.1	**0.7 ± 0.1**
	Type 1 and 2, $(r-4.5) < 6.1$ (Vega)	391	1.74	44.2	**0.7 ± 0.1**
	Type 1 and 2, $(r-4.5) < 6.1$ (Vega) $\log_{10}(L_{2-10}) > 44.4$	124	2.15	44.7	**0.7 ± 0.2**
	Type 1 and 2, $(r-4.5) > 6.1$ (Vega) $\log_{10}(L_{2-10}) > 44.4$	60	2.31	44.7	**1.2 ± 0.3**
	Type 1 and 2, $(r-K) > 5$ (Vega), $\log_{10}(X/0) > 1$	149	1.59	44.2	**0.7 ± 0.2**
	Type 1 and 2, $(r-K) > 5$ (Vega), $\log_{10}(X/0) > 1$ $\log_{10}(L_{2-10}) > 44.4$	31	1.96	44.7	**1.6 ± 0.4**
SED fit extinction	Type 1 and 2 $E(B-V)_{\mathrm{AGN}} > 0.3$	348	1.50	44.1	**0.7 ± 0.1**
	Type 1 and 2 $E(B-V)_{\mathrm{AGN}} < 0.3$	351	1.80	44.2	**0.7 ± 0.1**
	Type 1 and 2 $E(B-V)_{\mathrm{GAL}} > 0.3$	298	1.63	44.2	**0.9 ± 0.1**
	Type 1 and 2 $E(B-V)_{\mathrm{GAL}} < 0.3$	366	1.60	44.1	**0.7 ± 0.1**

4.4 Obscuration

AGN classifications into type 1s and type 2s as described in Section 2.2, are one way to potentially separate unobscured and obscured AGN. However, other obscuration measures have also previously been used in the literature, many of these tracing obscuration on potentially very different physical scales. A key aim of this work is to understand if any of these obscuration measures are correlated with the 850-µm flux and therefore SFRs of AGN. Having established trends in the 850-µm flux with both redshift and X-ray luminosity in the preceding sections, we will aim to disentangle these effects from the effects of obscuration on the cold dust emission.

4.4.1 Type 1 versus type 2 AGN

There are 428 $z > 1$ type 1 AGN and 271 $z > 1$ type 2 AGN in our sample as classified based on their spectroscopic properties/best-fitting SEDs (see Section 2.2). The median redshifts are 1.78 and 1.45 and the median hard X-ray luminosities are $\log_{10}(L_{2-10}) = 44.2$ and 44.0, respectively. In Appendix C, we also show both the X-ray luminosity and redshift distributions for the type 1 and type 2 populations. The type 2 population clearly shows a paucity of sources at the highest redshifts. However, in Section 4.2 we have already established that redshift trends are unlikely to be significant within the population. The stacked 850-µm flux densities for the type 1s and type 2s are 0.8 ± 0.1 and 0.6 ± 0.1 mJy, respectively. In Section 4.3, we have seen that the high luminosity type 2 AGN have higher submillimeter fluxes but at lower luminosities, the type 1 AGN 850-µm fluxes are slightly higher. Given that the X-ray luminosity distribution for the type 2 AGN sample peaks at lower luminosities than the type 1 AGN, this helps explain the small difference in the overall stacked fluxes observed here.

4.4.2 X-ray hardness ratio

The X-ray hardness ratio (HR) is used to characterize the colour index associated with the X-ray spectrum of an AGN and therefore the level of absorption seen in the X-ray. The HR is defined as $(H+S)/(H-S)$ where H represents the counts in the *XMM–Newton* hard X-ray band and S represents the counts in the *XMM–Newton* soft X-ray band. An HR value of −0.2 has been used by Brusa et al. (2010) to separate obscured and unobscured AGN and following this, we split our AGN sample into two HR bins. Only those AGN that are detected in *both* the soft and hard X-ray bands are used for this analysis. Our sample comprises 129 HR ≥ -0.2 obscured AGN (34 type 1 and 95 type 2) and 346 HR < -0.2 unobscured AGN (263 type 1 and 83 type 2). The average 850-µm fluxes are very similar for the obscured and unobscured samples as shown in Table 3 – 0.7 ± 0.3 mJy at HR ≥ -0.2 and 0.7 ± 0.1 mJy at HR < -0.2. In Appendix C, we also show the redshift and luminosity distributions for the two samples, which are very similar. Various previous studies have considered the dependence of cool dust emission from AGN on X-ray obscuration estimates parametrized by the neutral hydrogen column density (e.g. Stevens et al. 2005; Lutz et al. 2010; Shao et al. 2010; Rosario et al. 2012; Merloni et al. 2014). In most of these studies, no significant correlation is seen between cool dust emission and the dust column towards the central accreting black hole. Thus, the dust responsible for the X-ray absorption is probably not directly associated with star formation processes. Indeed, most X-ray studies place warm absorbers on much smaller spatial scales than typical star-forming regions in galaxies.

4.4.3 Optical-to-infrared colours

Optical to infrared flux ratios have been proposed as a way of identifying luminous obscured quasars that are not in X-ray surveys (e.g. Hickox et al. 2007) and recent results suggest that far-infrared fluxes and therefore SFRs could be correlated with such colour measures of obscuration (Chen et al. 2015). We therefore split our AGN sample into two (r–4.5 µm) colour bins using the threshold of (r–4.5 µm) = 6.1 (Vega) used in both Hickox et al. (2007) and Chen et al. (2015). The red sample has 303 AGN (65 type 1 and 238 type 2) at a median redshift of 1.56, whereas the blue sample has 391 AGN (359 type 1 and 32 type 2) at a median redshift of 1.74. The stacked 850-µm fluxes are presented in Table 3 and are very similar for the two populations – 0.7 ± 0.1 mJy.

Our result, that red and blue AGN have very similar submillimeter properties, is apparently at odds with that of Chen et al. (2015). However, these authors have investigated differences in red and blue AGN at the highest quasar luminosities. Lutz et al. (2010) also find that trends with obscuration start to become more significant at high X-ray luminosities and as illustrated in Fig. 6, differences in type 1 and type 2 AGN submillimeter fluxes only become significant at high luminosities. We therefore only select those AGN with $\log_{10}(L_{2-10}) > 44.4$ and again split these into two samples based on the $(r - 4.5\,\mu\mathrm{m})$ colours. The red sample has 60 AGN (18 type 1 and 42 type 2) and the blue sample has 124 AGN (116 type 1 and 8 type 2). The 850-µm fluxes in the two bins are once again given in Table 3. An excess in the 850-µm flux is now observed in the red AGN sample although this is only significant at the $\sim 1.3\sigma$ level given the sample size.

Another interesting population of red, dusty AGN have also been identified in the COSMOS field by Brusa et al. (2010). These authors use the $(r - K)$ colour and X-ray to optical flux ratio to select obscured AGN. Follow-up observations of this population demonstrate that they are hosted in starburst/main-sequence star-forming galaxies (Bongiorno et al. 2014) with strong evidence for powerful outflows affecting the ionized gas (Brusa et al. 2015; Cresci et al. 2015), consistent with these dusty quasars being caught during a brief evolutionary phase when both star formation and black hole accretion are synchronously occurring. The most X-ray luminous red AGN in the COSMOS field, XID2028, was independently selected in a wide-field search for reddened, high-redshift quasars in the UKIDSS Large Area Survey (Banerji et al. 2012). The population of hyper-luminous reddened quasars also shows evidence for very high dust luminosities (Banerji, Fabian & McMahon 2014) and large reservoirs of molecular gas (Feruglio et al. 2014), suggesting that the dust obscuration is, at least partially associated with star formation in the quasar host. This population of moderately obscured or reddened AGN appears to dominate the AGN luminosity function even at very high luminosities (Banerji et al. 2015; Lacy et al. 2015). These are therefore candidates where we might expect excess submillimeter emission relative to the rest of the AGN population.

The brightest red AGN XID2028 lies in a region of poor sensitivity in our 850-µm wide map, with $\sigma_{850} \sim 3.4$ mJy and is therefore not present in the 850-µm catalogue. XID18, another obscured quasar from Brusa et al. (2015), is associated with an 850-µm bright source in Table 1. We once again employ a stacking analysis in order to test whether such red obscured quasars are associated with high cold dust luminosities and therefore high SFRs. Specifically, we follow Brusa et al. (2010) and isolate a population of AGN with $(r{-}K) > 5$ (Vega) and $\log_{10}(\mathrm{X/O}) > 1$, where (X/O) represents the hard X-ray to optical r-band flux ratio and the monochromatic r-band flux is estimated as described in Brusa et al. (2010). Our sample comprises 149 AGN (14 type 1 and 135 type 2) at a median redshift of 1.59. The average 850-µm flux is 0.7 ± 0.2 mJy and there is no strong evidence for an excess in the submillimeter fluxes compared to the various other obscured populations that we have been investigating above. However, once again isolating only the X-ray luminous sub-set of this red population ($\log_{10}(L_{2-10}) > 44.4$), we now find that the stacked 850-µm flux of 1.6 ± 0.4 mJy to be more than two times higher at a significance of $\sim 2\sigma$, once again suggesting that an increase in cold dust emission with obscuration only becomes significant at high luminosities. While we have put forward the interpretation that the cold dust emission is directly tracing star formation in these high luminosity, obscured AGN samples, it is also possible that the more highly obscured X-ray luminous AGN simply have higher dust mass, which is responsible for driving the observed 850-µm emission trends. However, as dust mass in galaxies is closely tied to their gas content, large dust masses generally imply large gas reservoirs and therefore presumably also higher SFRs.

4.4.4 *E(B−V) from SED Fitting*

In Bongiorno et al. (2012), extinctions have been derived for the COSMOS AGN sample from SED fitting to the extensive multi-wavelength photometry. Separate extinction values were fit for the AGN and galaxy components. As expected the type 2 AGN are dominated by high extinctions towards the AGN component whereas the type 1 sources are fit by relatively modest extinctions to the AGN component. We begin by separating the $z > 1$ AGN sample based on these AGN component extinction values. Two samples are created with $E(B - V)_{\mathrm{AGN}} < 0.3$ and $E(B - V)_{\mathrm{AGN}} > 0.3$, respectively. The low extinction sample comprises 349 type 1 AGN and only two type 2 AGN and has a median redshift of 1.80 and a mean $E(B - V)_{\mathrm{AGN}} = 0.04$. The high extinction sample has 269 type 2 AGN and 79 type 1 AGN with a median redshift of 1.50 and a mean $E(B - V)_{\mathrm{AGN}} = 1.3$. The average 850-µm fluxes are 0.7 ± 0.1 mJy in both the low and high extinction bins, respectively, and there is therefore no evidence for a dependence of SFR on these AGN component extinction values.

We now consider the extinction values fit to the galaxy component instead, using a threshold of $E(B - V)_{\mathrm{GAL}} = 0.3$ to separate the AGN into two samples. The reliability of SED-based extinction estimates for AGN host galaxies has not been explored in detail thus far and should clearly be interpreted with caution, particularly for type 1 AGN. Before using these extinction values, we therefore look for systematic biases in the two populations. First, we confirm using the rest-frame monochromatic UV-luminosities from Lusso et al. (2010) for the type 1 AGN, that there are no systematic differences in the UV-luminosity between the two extinction bins ($\log_{10}(L_{\mathrm{UV}}/\mathrm{erg\,s^{-1}\,cm^{-2}\,Hz^{-1}}) = 29.7$ in both bins). Next we calculate the rest-frame 5.8-µm luminosity directly from the infrared photometry from Brusa et al. (2010) and look for differences in the mid-infrared luminosity between the two extinction bins. A systematic difference in the rest-frame 5.8-µm luminosity between host galaxy extinction bins would indicate that AGN split by their host galaxy extinction have different mid-infrared SEDs, which could reflect differences in covering factor and viewing angle. Once again, we find no notable difference in the rest-frame 5.8-µm luminosity as a function of extinction, with average values of $\log_{10}(L_{5.8}/\mathrm{erg\ s^{-1}}) = 45.1$ in both bins.

Having confirmed that the type 1 AGN split by host extinction do not show systematic differences in either their UV or IR luminosities, we now proceed to look at the average 850-µm flux in these two bins. The average fluxes are quoted in Table 3 and are 0.7 ± 0.1 and 0.9 ± 0.1 mJy in the low and high extinction bins, respectively. The mean $E(B{-}V)_{\mathrm{GAL}}$ values in these bins are 0.06 and 0.6, respectively. The excess 850-µm flux in the high extinction bin is only significant at the 1.4σ level. The median stellar masses and hard X-ray luminosities of the AGN in these two extinction bins are very similar – $\log_{10}(M_*/\mathrm{M_\odot}) = 10.80$ and 10.85, respectively and $\log_{10}(L_{2-10}/\mathrm{erg\,s^{-1}}) = 44.14$ and 44.16, respectively. The luminosity and redshift distributions of the various $E(B{-}V)$ selected samples are also shown in Appendix C and demonstrate that the samples overlap significantly in both X-ray luminosity and redshift space.

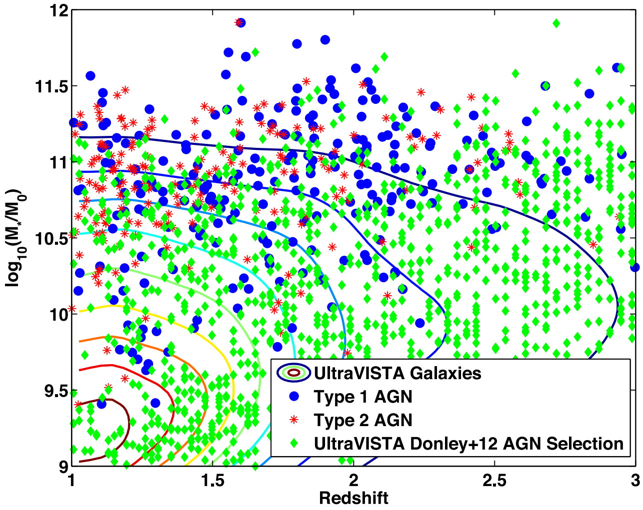

Figure 7. Redshift versus stellar mass of ∼114 000 UltraVISTA galaxies at $z > 1$ from Muzzin et al. (2013) compared to the type 1 and type 2 AGN (Bongiorno et al. 2012). In the case of the UltraVISTA galaxies, the coloured contours represent the density of points on the plot with red contours corresponding to the highest density. UltraVISTA galaxies that satisfy the Donley et al. (2012) IRAC AGN selection criteria are also shown and occupy the full redshift–mass plane. On the other hand, the X-ray AGN host galaxies correspond to the most massive end of the UltraVISTA galaxy stellar mass distribution at $z > 1$.

Overall, we find that trends in the 850-μm flux with different measures of obscuration are weak when the AGN sample is considered as a whole. However, we do find that these trends become more significant at the highest luminosities where a transition from secular to merger-driven co-evolution may be occurring. Much larger samples over wider fields are required to confirm these results and investigate the overlap between obscured populations selected using different classification methods. Starting with mid-infrared rather than X-ray-selected parent AGN samples would also help in getting better statistics on luminous, obscured AGN where high levels of obscuration cause the AGN to drop out of flux-limited X-ray samples. These studies are now becoming possible with very large mid-infrared surveys such as the *WISE* All-Sky Survey (Wright et al. 2010).

4.5 AGN versus non-AGN

Finally, we would like to understand if there is evidence for cool dust emission being preferentially associated with AGN activity or whether all galaxies of similar mass and at similar redshift, show similar dust emission properties. Stellar masses are available for both the type 1 and type 2 AGN samples from SED fitting (Bongiorno et al. 2012). The stellar masses as a function of redshift are shown in Fig. 7. As described in Section 4.5, we also have a control sample of galaxies from the UltraVISTA survey with photometric redshifts and stellar masses from Muzzin et al. (2013). The stellar mass versus redshift distribution for ∼114 000 galaxies selected from this sample is also shown in Fig. 7. In both cases, the stellar masses have been computed using the Bruzual & Charlot (2003) stellar population synthesis models with a Chabrier (2003) initial mass function and assuming exponentially declining star formation histories so the two stellar mass estimates should be comparable. Matching the UltraVISTA galaxy catalogue to the Bongiorno et al. (2012) catalogue, we find that for the type 2 AGN sample, where the emission is dominated by the galaxy SED and the contribution from the AGN template is negligible, the stellar masses in the two catalogues agree to within 0.1 dex with a median difference of 0.08 dex in the masses. In the analysis that follows, we separate sources into stellar mass bins of width 0.5 dex so for our purposes, differences in stellar masses between Bongiorno et al. (2012) and Muzzin et al. (2013) are negligible.

From Fig. 7, it is apparent that the AGN host galaxy masses are at the top end of the distribution of masses in the UltraVISTA galaxy population. We therefore begin by selecting both samples of galaxies and AGN to be in the stellar mass range $10.0 < \log_{10}(M_*/\mathrm{M}_\odot) < 11.5$ and require the AGN stellar masses to have *flag 0* in the catalogue of Bongiorno et al. (2012), which indicates that these stellar mass estimates are robust. In the case of the type 1 AGN, these *flag* 0 sources correspond to those where the galaxy contribution at 1 μm is >10 per cent so the mass of the galaxy can effectively be constrained (Merloni et al. 2010; Bongiorno et al. 2012). We also restrict our analysis to only those AGN with errors of <0.1 dex on their stellar masses. In order to remove any contamination from AGN in the non-AGN galaxy sample, we cross-match the UltraVISTA galaxies to the *XMM–Newton* point-source catalogue of Cappelluti et al. (2009) and remove any galaxies associated with an X-ray point source within a matching radius of 8 arcsec. Even within the mass range selected for our AGN versus non-AGN galaxy comparison study, the mass distribution for the AGN is more strongly skewed towards higher masses than the corresponding galaxy distribution. As it is well known that more massive galaxies have higher SFRs, this can introduce biases into our analysis. Starting with the non-AGN, we therefore match both the mass and redshift distributions of the galaxies to that of the AGN by randomly sampling from the galaxies in $\delta\log(M_*)$ bins of width 0.1 and δz bins of width 0.1. The number of AGN to non-AGN in each mass bin is fixed to be the same and we therefore ensure that the median stellar mass of the non-AGN galaxy sample is the same as that of the AGN sample – $\log_{10}(M_*/\mathrm{M}_\odot) = 10.9$ in both cases. The median redshifts are 1.66 for the AGN and 1.68 for the non-AGN. A potential concern is that highly obscured AGN that are not detected in the X-ray, still remain in the non-AGN galaxy sample. However, visual inspection of the best-fitting galaxy SEDs from Muzzin et al. (2013) confirms that the majority of these galaxies do not have power-law-type AGN-dominated SEDs in the *Spitzer* IRAC bands. From our sample of 782 mass-matched non-AGN galaxies, we find that <5 per cent satisfy the IRAC AGN selection criteria presented by Donley et al. (2012). As illustrated in Fig. 7, UltraVISTA galaxies that satisfy the Donley et al. (2012) AGN selection criteria, occupy the entire redshift–mass plane and do not dominate at high masses. In this high-mass regime, the UltraVISTA galaxies are therefore unlikely to suffer from heavy contamination from highly obscured AGN.

With the mass and redshift distributions of the inactive galaxies and AGN now matched, we proceed to calculating their average 850-μm fluxes. The non-AGN galaxy sample has a higher 850-μm flux compared to the AGN – 1.01 ± 0.09 mJy versus 0.72 ± 0.12 mJy. The median and mean 850-μm fluxes for both the AGN and non-AGN are also consistent with each other confirming that the stacked properties are not being dominated by a few outliers. To investigate this excess in more detail, we now split our galaxy and AGN sample into three stellar mass bins and consider the type 1 and type 2 AGN populations independently. The average submillimeter fluxes in the three stellar mass bins are presented in Table 4 and illustrated in Fig. 8. While the type 2 AGN 850-μm fluxes increase as a function of stellar mass, the type 1 AGN fluxes remain fairly constant. The redshift and luminosity distributions of the AGN in all three stellar

Table 4. Stacked 850-µm fluxes for the type 1 and type 2 AGN and a sample of non-AGN galaxies selected from UltraVISTA in three stellar mass bins. Detections above 3σ are shown in bold and the number of sources in each bin is given in brackets.

	Type 1 AGN	Type 2 AGN	Non-AGN UltraVISTA Galaxies
$10.0<\log_{10}(M_*/\mathrm{M}_\odot) < 10.5$	0.6 ± 0.3 mJy ($N = 35$)	0.3 ± 0.4 mJy ($N = 22$)	**0.6 ± 0.2 mJy** ($N = 98$)
$10.5<\log_{10}(M_*/\mathrm{M}_\odot) < 11.0$	**1.0 ± 0.3 mJy** ($N = 97$)	0.4 ± 0.2 mJy ($N = 91$)	**0.8 ± 0.1 mJy** ($N = 329$)
$11.0<\log_{10}(M_*/\mathrm{M}_\odot) < 11.5$	**1.0 ± 0.2 mJy** ($N = 91$)	**0.9 ± 0.2 mJy** ($N = 69$)	**1.4 ± 0.1 mJy** ($N = 355$)

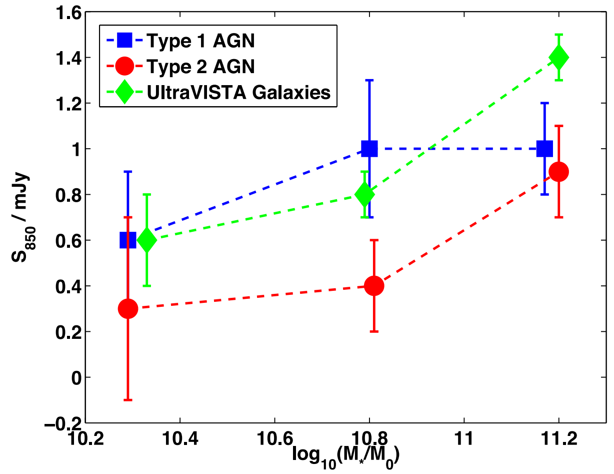

Figure 8. Average 850-µm flux versus stellar mass for both type 1 and type 2 AGN and compared to a sample of non-AGN galaxies selected from the UltraVISTA survey.

mass bins can be seen in Appendix C. In the case of both the type 1 and type 2 AGN, the highest stellar mass bins peak at higher X-ray luminosities consistent with more massive galaxies having more powerful accreting black holes. Combined with the results in Fig. 6, this suggests that the trends in submillimeter emission with mass are equivalent to the trends with X-ray luminosity, with type 1 AGN showing little evolution and high-luminosity/high-mass type 2 AGN being more submillimeter bright. Interestingly however, the galaxy stacked fluxes are in general comparable to or higher than those seen in the AGN population. For type 2 AGN, this appears to be the case over pretty much the entire mass range probed. Non-AGN hosts therefore appear to be more highly star forming than the X-ray AGN.

These results are somewhat at odds with similar analyses conducted using *Herschel* data where evidence for excess star formation is seen in AGN host galaxies relative to non-AGN host galaxies of similar mass (e.g. Santini et al. 2012). The excess disappears when considering star-forming galaxies only leading the authors to conclude that AGN are preferentially hosted in star-forming galaxies with the same gas supply likely fuelling both processes. However, we note that in contrast to these investigations, Bongiorno et al. (2012) find that AGN are preferentially hosted in redder, more quiescent galaxies. Bongiorno et al. (2012) have already pointed out that their SED-fitting method, by correcting for dust extinction to both the AGN and host galaxy components and disentangling the UV-luminous AGN emission from that from star formation, leads to lower SFR estimates for AGN hosts relative to Santini et al. (2012). The AGN template used by Santini et al. (2012) is a Seyfert template. While this is clearly appropriate for low-luminosity AGN, for the high-luminosity *XMM*-COSMOS AGN investigated here, it may not account for all the UV emission from the AGN, therefore leading to an overestimate of the SFR.

The higher average 850-µm flux of the non-AGN galaxy sample is primarily driven by the most massive galaxies with $\log_{10}(M_*/\mathrm{M}_\odot) > 11.0$ as can be seen in Fig. 8. These most massive galaxies have extremely red SEDs with very little flux at rest-frame UV wavelengths. Many of these ultrared galaxies would not be selected in flux-limited catalogues generated in bluer bands such as the *r* or *i* band and could be one reason for the different conclusions from our analysis and that of e.g. Santini et al. (2012). Interpreting the higher 850-µm fluxes of the Muzzin et al. (2013) massive galaxies as signifying that they have higher SFRs relative to AGN, requires us to assume that the average dust properties are similar in both populations. Inspection of the best-fitting non-AGN galaxy SEDs at $\log_{10}(M_*/\mathrm{M}_\odot) > 11.0$ from Muzzin et al. (2013) however confirms that these galaxies are almost always fit by highly star-forming galaxy templates with significant extinction (median $A_\mathrm{V} = 0.9$), lending credence to the idea that a significant fraction of the massive galaxies found by Muzzin et al. (2013) at these redshifts may indeed correspond to starburst galaxies with very high SFRs and therefore submillimeter fluxes.

We have shown that AGN host galaxies appear to have lower 850-µm fluxes compared to a mass-matched sample of non-AGN galaxies. It is important to highlight that photometric redshifts as well as stellar masses for both the AGN and non-AGN samples are clearly model dependent and affected by the choice of templates used in the SED fitting. Stellar mass estimates are also likely to be less reliable for type 1 AGN where the host galaxy is less visible. However, as can be seen in Fig. 8, it is the difference between the submillimeter fluxes of type 2 AGN hosts and non-AGN that is more significant. Different model choices in SED fitting could perhaps partially explain the different conclusions reached regarding the nature of AGN host galaxies in the literature. However, another key issue is that many previous studies have selected non-AGN galaxy samples from optical survey data, which are less sensitive to star-forming galaxies with significant dust extinctions. High-mass, high-redshift, red populations of non-AGN galaxies that are matched in mass to the most luminous AGN are now selectable using new deep infrared surveys such as UltraVISTA that cover reasonably wide fields. Due to their rarity, these massive red galaxies are only present in wide-field extragalactic surveys such as COSMOS and due to the red colours of this population, they are often not present in optical flux-limited surveys. These galaxies are also the most difficult to obtain spectra of. Understanding their true nature – i.e. whether they correspond to massive dusty starbursts – is now vital in order to be able to relate them to the AGN host galaxies which have equivalently high stellar masses.

5 CONCLUSIONS

We have studied the 850-µm properties of X-ray-selected AGN in the COSMOS field using new data from the S2CLS. The 850-µm data covering ~2 deg^2 presents an opportunity to study the cold dust emission from a statistically significant number of luminous AGN as a function of properties such as luminosity, stellar mass and obscuration. We begin by searching for AGN that are detected at $>3.5\sigma$ in our 850-μm data in a 'high sensitivity' (σ_{850} <2 mJy) region covering 0.89 $\deg^2$. There are 360 submillimeter sources over this area and we identify that 19 of these are X-ray luminous AGN. These submillimeter galaxies have S_{850} = 4–10 mJy. The 19 submillimeter-detected X-ray AGN comprise six spectroscopically confirmed broad-line AGN, one spectroscopically confirmed narrow-line AGN, three photometric redshift AGN that are best fit by type 1 AGN templates and nine photometric redshift AGN that are best fit by type 2 or galaxy templates. In terms of X-ray luminosity, these AGN fill the luminosity gap between the very X-ray luminous quasars that have been individually followed up at submillimeter wavelengths (e.g. Stevens et al. 2005) and sub-mm-detected X-ray AGN from much smaller area, deeper X-ray surveys (e.g. Alexander et al. 2005; Wang et al. 2013).

We construct inverse-variance weighted stacked 850-μm images of different sub-samples of $z > 1$ AGN in the X-ray luminosity range $43 \lesssim \log_{10}(L_X) \lesssim 45$, utilizing a hard X-ray (2–10 keV) flux-limited population of 699 radio quiet AGN (428 type 1 and 271 type 2). The average 850-μm fluxes are measured from a 100 such bootstrap images and for the entire AGN population, $S_{850} = 0.71 \pm 0.08$ mJy. The 850-μm flux directly traces the dust luminosity at $z > 1$ due to the effects of the negative k-correction so the 850-μm fluxes can be averaged over relatively wide redshift bins at these high redshifts. Under the assumption of an isothermal SED, the 850-μm flux can therefore be used as a proxy for SFR. Using independent estimates of the SFR in the COSMOS AGN sample estimated via SED fitting to the optical through infrared photometry, we demonstrate that AGN with higher SFRs do, on average, have higher 850-μm fluxes. In particular, AGN with SFR > 10 $M_\odot$ yr^{-1} have 850-μm fluxes that are ~3.3 times higher than those in AGN with SFR < 10 $M_\odot$ yr^{-1}. We then study the dependence of this 850-μm flux on various AGN properties. In particular, we reach the following conclusions.

(i) The 850-μm fluxes of both type 1 and type 2 AGN show little evolution with redshift and the type 1 and type 2 AGN have average submillimeter fluxes that are consistent with each other over the entire redshift range probed in this study.

(ii) We study the dependence of 850-μm emission and therefore star formation on AGN X-ray luminosity. We find that the 850-μm fluxes are relatively constant for $z > 1$ type 1 AGN at $\log_{10}(L_{2-10}) > 43.5$. However, in the case of the $z > 1$ type 2 AGN, we find that the 850-μm flux increases with X-ray luminosity. This may suggest a transition from secular to merger-driven evolution in the type 2 AGN population at the highest X-ray luminosities ($\log_{10}(L_{2-10}) > 44.4$) probed in this work, which could be responsible for the tighter coupling seen between cold dust emission (tracing star formation) and X-ray luminosity (tracing black hole accretion) at these luminosities. Our results also indicate that high-luminosity type 1 and type 2 AGN have systematic differences in their observed 850-μm flux densities, which could reflect systematic differences in their host galaxy properties with the type 2 AGN occupying more highly star-forming galaxies. Alternatively, the higher 850-μm flux densities in high luminosity type 2 AGN could simply arise as a result of these AGN having higher dust mass relative to type 1 AGN of comparable luminosity.

(iii) Having explored trends with redshift and luminosity, we study the dependence of submillimeter flux on obscuration, relying on various different obscuration measures. There is no significant dependence of the 850-μm flux on X-ray HR or the (r–4.5 μm) colour when averaging over all X-ray luminosities. When selecting the most X-ray luminous AGN ($\log_{10}(L_{2-10}) > 44.4$), we find that the red AGN have submillimeter fluxes that are ~1.7 times higher than the blue AGN, although given the sample size, the result is only significant at the $\sim 1.3\sigma$ level.

(iv) Following Brusa et al. (2010), we select a population of red ($r - K$) AGN with high X-ray to optical flux ratios. Once again these AGN have very similar submillimeter properties to the rest of the AGN population when averaging over all X-ray luminosities. However in the highest X-ray luminosity bin ($\log_{10}(L_{2-10}) > 44.4$), these red AGN have submillimeter fluxes that are more than a factor of 2 higher than the average. Despite the small samples in this single field, the results are still significant at the $\sim 2\sigma$ level and consistent with a more marked dependence of submillimeter emission on obscuration for the most X-ray luminous AGN.

(v) Finally, the $z > 1$ AGN are compared to a K-band-selected population of galaxies showing no evidence for AGN activity and that are carefully matched in stellar mass and redshift to the AGN sample. On account of the K-band selection, this non-AGN galaxy sample includes populations of extremely red galaxies at the high-mass end, many of which have very little flux at rest-frame UV wavelengths and would not be selected in optical flux-limited surveys. Type 2 AGN show an increase in submillimeter flux with stellar mass which is equivalent to the increase seen as a function of X-ray luminosity. Over almost the entire mass range probed however, non-AGN have higher 850-μm fluxes compared to the type 2 AGN and in the highest stellar mass bin – 11.0 $< \log_{10} <$ 11.5 – the non-AGN also have higher submillimeter fluxes compared to the type 1 AGN. The best-fitting SED templates for the massive non-AGN galaxies indicate that they are dusty galaxies with high star formation rates and a median A_V of 0.9. Such massive, red non-AGN galaxies have eluded discovery in previous surveys that have either covered smaller areas or been flux-limited in the bluer optical bands. Due to their red colours, many of these galaxies also remain spectroscopically unconfirmed. Understanding their true nature is important to be able to relate them to their AGN counterparts of equivalent mass.

We have demonstrated the unique sensitivity and resolution of the new SCUBA-2 850-μm data provided by the S2CLS, which has allowed us to probe rest-frame wavelengths corresponding to the Rayleigh Jeans tail in the SEDs of luminous X-ray AGN in the high-redshift Universe. At these wavelengths, the 850-μm emission provides a unique probe of the cold dust luminosity and dust mass in AGN samples. Although the sample size used in this work has limited the significance of some of our results, nevertheless we find some evidence for a stronger coupling between AGN luminosity, dust luminosity and obscuration at high X-ray luminosities, where we may be seeing a transition from a secular to a merger-driven regime in galaxy evolution. Larger samples of AGN selected at multiple wavelengths are clearly required to establish more significant trends in the star formation properties of AGN host galaxies across a wide range in luminosity, redshift and mass. This will become possible when similar analyses are extended to cover all the fields imaged by the S2CLS.

ACKNOWLEDGEMENTS

We thank the referee for a constructive review that helped improve the current analysis. We thank James Aird, Paul Hewett and Adam Muzzin for useful discussions, Angela Bongiorno for kindly providing the errors on the AGN stellar mass estimates and Ian Smail for helpful comments on the manuscript. MB, RGM and KEKC acknowledge support from STFC. JEG thanks the Royal Society for a University Research Fellowship. NB and JSD acknowledge the support of the European Research Council via the award of an Advanced Grant, and the contribution of the EC FP7 SPACE project ASTRODEEP (Ref. No: 312725). DMA and CMH acknowledge support from STFC grant ST/I001573/1.

This work was carried out based on observations obtained using SCUBA-2 on the JCMT. The JCMT has historically been operated by the Joint Astronomy Centre on behalf of the Science and Technology Facilities Council of the United Kingdom, the National Research Council of Canada and the Netherlands Organization for Scientific Research. Additional funds for the construction of SCUBA-2 were provided by the Canada Foundation for Innovation.

REFERENCES

Aird J. et al., 2013, ApJ, 775, 41
Aird J., Coil A. L., Georgakakis A., Nandra K., Barro G., Pérez-González P. G., 2015, MNRAS, 451, 1892
Alexander D. M., Hickox R. C., 2012, New Astron. Rev., 56, 93
Alexander D. M., Bauer F. E., Chapman S. C., Smail I., Blain A. W., Brandt W. N., Ivison R. J., 2005, ApJ, 632, 736
Antonucci R., 1993, ARA&A, 31, 473
Azadi M. et al., 2015, ApJ, 806, 187
Banerji M., McMahon R. G., Hewett P. C., Alaghband-Zadeh S., Gonzalez-Solares E., Venemans B. P., Hawthorn M. J., 2012, MNRAS, 427, 2275
Banerji M., Fabian A. C., McMahon R. G., 2014, MNRAS, 439, L51
Banerji M., Alaghband-Zadeh S., Hewett P. C., McMahon R. G., 2015, MNRAS, 447, 3368
Blain A. W., Smail I., Ivison R. J., Kneib J.-P., Frayer D. T., 2002, 369, 111
Bonfield D. G. et al., 2011, MNRAS, 416, 13
Bongiorno A. et al., 2012, MNRAS, 427, 3103
Bongiorno A. et al., 2014, MNRAS, 443, 2077
Bourne N. et al., 2013, MNRAS, 436, 479
Brightman M., Nandra K., Salvato M., Hsu L.-T., Aird J., Rangel C., 2014, MNRAS, 443, 1999
Brusa M. et al., 2010, ApJ, 716, 348
Brusa M. et al., 2015, MNRAS, 446, 2394
Bruzual G., Charlot S., 2003, MNRAS, 344, 1000
Cappelluti N. et al., 2009, A&A, 497, 635
Casey C. M., 2012, MNRAS, 425, 3094
Casey C. M. et al., 2013, MNRAS, 436, 1919
Chabrier G., 2003, PASP, 115, 763
Chapin E. L., Berry D. S., Gibb A. G., Jenness T., Scott D., Tilanus R. P. J., Economou F., Holland W. S., 2013, MNRAS, 430, 2545
Chen C.-T. J. et al., 2015, ApJ, 802, 50
Cresci G. et al., 2015, ApJ, 799, 82
Croton D. J. et al., 2006, MNRAS, 365, 11
Di Matteo T., Springel V., Hernquist L., 2005, Nature, 433, 604
Donley J. L. et al., 2012, ApJ, 748, 142
Feruglio C. et al., 2014, A&A, 565, A91
Gabor J. M., Bournaud F., 2013, MNRAS, 434, 606
Geach J. E. et al., 2013, MNRAS, 432, 53
Hao H. et al., 2014, MNRAS, 438, 1288
Harrison C. M. et al., 2012, ApJ, 760, L15
Hickox R. C. et al., 2007, ApJ, 671, 1365
Hickox R. C., Mullaney J. R., Alexander D. M., Chen C.-T. J., Civano F. M., Goulding A. D., Hainline K. N., 2014, ApJ, 782, 9
Ivison R. J. et al., 2007, MNRAS, 380, 199
Kormendy J., Ho L. C., 2013, ARA&A, 51, 511
Lacy M., Ridgway S. E., Sajina A., Petric A. O., Gates E. L., Urrutia T., Storrie-Lombardi L. J., 2015, ApJ, 802, 102
Lusso E. et al., 2010, A&A, 512, A34
Lusso E. et al., 2011, A&A, 534, A110
Lutz D. et al., 2008, ApJ, 684, 853
Lutz D. et al., 2010, ApJ, 712, 1287
McCracken H. J. et al., 2012, A&A, 544, A156
Magorrian J. et al., 1998, AJ, 115, 2285
Merloni A. et al., 2010, ApJ, 708, 137
Merloni A. et al., 2014, MNRAS, 437, 3550
Mullaney J. R. et al., 2012, MNRAS, 419, 95
Muzzin A. et al., 2013, ApJS, 206, 8
Oliver S. J. et al., 2012, MNRAS, 424, 1614
Page M. J., Stevens J. A., Mittaz J. P. D., Carrera F. J., 2001, Science, 294, 2516
Page M. J., Stevens J. A., Ivison R. J., Carrera F. J., 2004, ApJ, 611, L85
Page M. J. et al., 2012, Nature, 485, 213
Richards G. T. et al., 2006, AJ, 131, 2766
Rosario D. J. et al., 2012, A&A, 545, A45
Rovilos E. et al., 2012, A&A, 546, A58
Salvato M. et al., 2009, ApJ, 690, 1250
Salvato M. et al., 2011, ApJ, 742, 61
Sanders D. B. et al., 2007, ApJS, 172, 86
Santini P. et al., 2012, A&A, 540, A109
Schinnerer E. et al., 2010, ApJS, 188, 384
Scoville N. et al., 2007, ApJS, 172, 1
Shao L. et al., 2010, A&A, 518, L26
Sijacki D., Vogelsberger M., Genel S., Springel V., Torrey P., Snyder G., Nelson D., Hernquist L., 2015, MNRAS, 452, 575
Springel V., Di Matteo T., Hernquist L., 2005, ApJ, 620, L79
Stanley F., Harrison C. M., Alexander D. M., Swinbank A. M., Aird J. A., Del Moro A., Hickox R. C., Mullaney J. R., 2015, MNRAS, 453, 591
Stevens J. A., Page M. J., Ivison R. J., Carrera F. J., Mittaz J. P. D., Smail I., McHardy I. M., 2005, MNRAS, 360, 610
Swinbank A. M. et al., 2014, MNRAS, 438, 1267
Symeonidis M. et al., 2014, MNRAS, 443, 3728
Urry C. M., Padovani P., 1995, PASP, 107, 803
Viero M. P. et al., 2013, ApJ, 779, 32
Wang S. X. et al., 2013, ApJ, 778, 179
Wright E. L. et al., 2010, AJ, 140, 1868

APPENDIX A: X-RAY LUMINOSITIES AND ABSORPTION CORRECTIONS

When deriving hard X-ray luminosities for our AGN sample in Section 2.2, we have neglected the effects of absorption. Significant

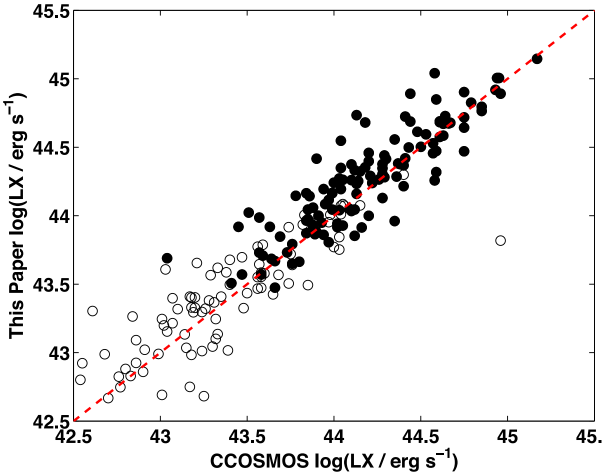

Figure A1. Hard X-ray luminosities derived in this paper (Section 2.2) versus those derived using *Chandra* data by Brightman et al. (2014) and including the effects of absorption. Filled circles correspond to AGN at $z > 1$ which are used for all the stacking analysis considered in this work. No systematic bias is seen in our X-ray luminosities compared to the absorption corrected X-ray luminosities of Brightman et al. (2014), confirming that absorption has a negligible impact on the derived luminosities for the majority of our sample.

absorption in a large fraction of our sample would systematically bias our X-ray luminosity estimates. As illustrated in fig. 5 of Aird et al. (2015) however, hard X-ray luminosities are only likely to be significantly biased for absorbing columns of $N_{\mathrm{H}} > 10^{23}$ cm^{-2}. A subset of the COSMOS AGN considered in this work also have deep X-ray observations obtained using the *Chandra* observatory and where the data is of sufficient quality to enable detailed spectral fitting including different absorption components. Brightman et al. (2014) have conducted exactly such a study and derived absorption corrected hard X-ray luminosities as well as column densities for the X-ray AGN. We therefore match our sample of X-ray AGN to the Brightman et al. (2014) sample. There are 217 AGN in common between the two catalogues and where the redshifts in both catalogues also agree. In Fig. A1, we compare the hard X-ray luminosities derived in this paper (without absorption correction) to the hard X-ray luminosities from Brightman et al. (2014). As can be seen, most of the AGN lie on the $x = y$ relation and the median difference between our X-ray luminosities and those of Brightman et al. (2014) is 0.06 dex. When considering the dependence of submillimeter flux on hard X-ray luminosity, we stack sub-samples in bins of 0.4–0.5 dex in X-ray luminosity. Hence, we conclude that any biases in our X-ray luminosities due to a lack of absorption correction, are unlikely to significantly affect the trends observed in this paper.

APPENDIX B: PROPERTIES OF 850-μm DETECTED X-RAY AGN

In this section, we present the properties of our sample of 19 X-ray AGN that are associated with 850-μm sources in the COSMOS field. Table B1 presents the stellar masses and various obscuration parameters investigated in this work for each of the 19 AGN. Table B2 presents photometry from *Spitzer* MIPS (24 μm), *Herschel* PACS (100 and 160 μm) and SPIRE (250, 350 and 500 μm). In Fig. B1, we show the best-fitting SEDs for the AGN that are detected in at least two of the *Herschel* bands. We fit a power law of the form $S_\lambda \propto \lambda^\alpha$ to model the mid-infrared emission from the AGN at $\lambda \gtrsim 3$ μm,

Table B1. Summary of the properties of the 19 X-ray AGN that are associated with 850-μm sources. Note: the hard X-ray luminosities and redshifts of these sources are presented in Table 1.

XID	$\log_{10}(M_*/\mathrm{M}_\odot)$	HR	(r−4.5 μm) Vega	$E(B-V)_{\mathrm{AGN}}$	$E(B-V)_{\mathrm{GAL}}$
13	11.26	−0.58	5.44	0.1	0.0
18	11.17	−0.21	7.68	0.6	0.0
139	10.08	−0.37	6.61	0.6	0.2
160	10.61	−0.09	5.18	0.8	0.2
246	9.12	0.42	8.59	1.3	0.3
250	11.11	–	5.02	0.1	0.5
270	11.74	–	8.13	0.3	0.3
278	11.26	–	9.13	2.6	0.5
353	11.24	−0.14	6.28	0.0	0.4
402	10.54	−0.24	6.57	0.3	0.4
415	9.92	–	6.18	0.3	0.5
469	10.44	–	6.00	0.3	0.1
10675	11.16	–	5.37	1.0	0.1
10809	10.09	–	6.56	0.4	0.0
30182	9.62	−0.6	3.82	0.3	0.0
53922	9.25	−0.16	6.66	2.3	0.2
54440	11.18	–	9.07	0.7	0.5
60070	11.32	–	7.99	0.4	0.5
60490	10.66	–	6.57	0.3	0.0

Table B2. Summary of *Spitzer* MIPS and *Herschel* fluxes of the 19 X-ray AGN that are associated with 850-μm sources. Note: the SCUBA-2 850-μm flux densities of these sources are presented in Table 1.

XID	S_{24}/mJy	S_{100}/mJy	S_{160}/mJy	S_{250}/mJy	S_{350}/mJy	S_{500}/mJy
13	0.91 ± 0.06	–	–	13.8 ± 2.8	34.4 ± 5.2	23.9 ± 4.8
18	0.51 ± 0.02	–	–	<9.2	<10.6	<12.2
139	2.27 ± 0.37	18.4 ± 2.9	55.7 ± 3.0	59.6 ± 6.5	45.7 ± 5.9	31.3 ± 5.7
160	1.59 ± 0.12	29.3 ± 2.1	75.2 ± 3.2	69.3 ± 7.0	51.6 ± 6.2	29.0 ± 5.4
246	0.88 ± 0.02	–	–	<9.0	<12.1	<12.6
250	0.28 ± 0.02	4.9 ± 1.2	–	<9.2	<10.6	<12.2
270	0.87 ± 0.02	13.7 ± 1.6	31.3 ± 3.1	53.3 ± 6.0	48.8 ± 6.0	22.5 ± 5.0
278	0.56 ± 0.02	–	14.9 ± 3.5	18.3 ± 3.2	21.9 ± 4.1	16.2 ± 3.6
353	0.40 ± 0.02	–	12.5 ± 2.9	16.8 ± 3.1	<16.1	<16.3
402	0.28 ± 0.09	–	13.3 ± 3.3	<14.6	<15.9	<13.6
415	0.13 ± 0.02	–	–	<9.2	<10.6	<12.2
10675	0.09 ± 0.02	–	–	<9.2	<10.3	<12.6
53922	1.24 ± 0.03	10.7 ± 1.8	35.2 ± 3.7	36.4 ± 4.9	34.7 ± 5.2	–
54440	0.39 ± 0.02	–	15.7 ± 3.8	27.1 ± 4.1	27.2 ± 4.7	<16.3
60070	0.34 ± 0.05	–	9.3 ± 3.0	12.5 ± 2.6	<13.9	<13.6
60490	0.08 ± 0.02	–	–	<10.0	<15.2	<12.2

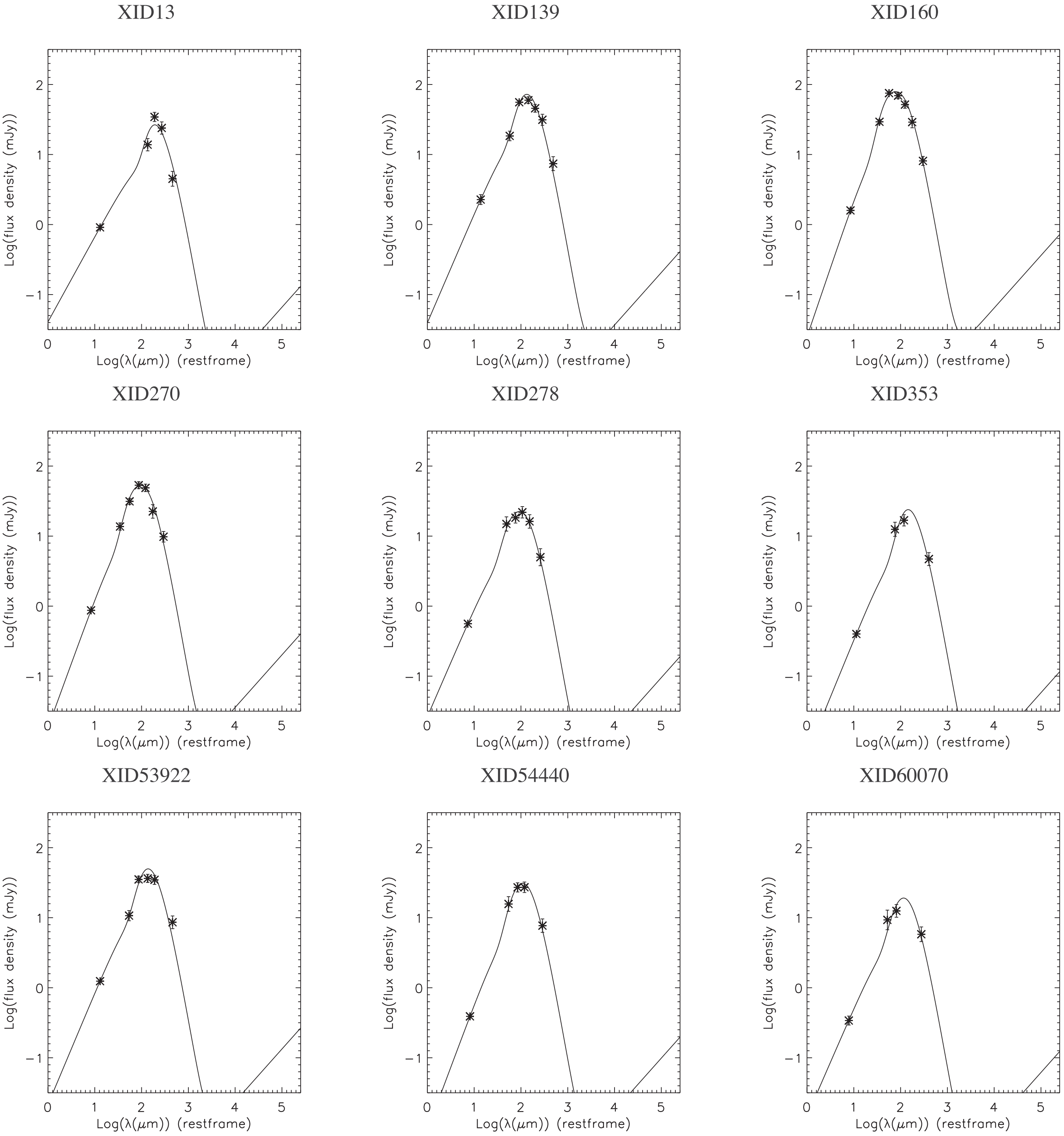

Figure B1. Best-fitting SEDs for the nine AGN in Table B2 with at least two detections in the *Herschel* bands.

together with a single temperature greybody (Casey 2012) with a fixed dust emissivity index of $\beta = 2$. The best-fitting mid-infrared power-law slope, α, dust temperature, far-infrared luminosity (60–300 μm) and dust mass are given in Table B3. In Fig. B2, we also show the correlation between the far-infrared luminosity and the 250- and 850-μm fluxes for these individually detected AGN as well as the correlation between the 250- and 850-μm fluxes and the dust mass.

Table B3. Best-fitting SED parameters for individually detected AGN with at least two detections in the *Herschel* bands.

XID	$\alpha_{\rm MIR}$	$T_{\rm dust}/K$	$\log_{10}(L_{\rm FIR}/{\rm L}_{\odot})$	$\log_{10}(M_{\rm dust}/{\rm M}_{\odot})$
13	1.21 ± 0.07	15 ± 2	11.41 ± 0.16	9.08 ± 2.41
139	1.55 ± 0.09	22 ± 1	11.85 ± 0.09	8.56 ± 0.34
160	1.97 ± 0.06	37 ± 2	12.70 ± 0.05	8.58 ± 0.07
270	1.84 ± 0.04	31 ± 2	12.57 ± 0.07	8.73 ± 0.07
278	1.54 ± 0.08	32 ± 5	12.34 ± 0.14	8.52 ± 0.08
353	1.63 ± 0.07	20 ± 2	11.69 ± 0.15	8.70 ± 0.15
53922	1.59 ± 0.04	21 ± 2	11.80 ± 0.10	8.62 ± 0.21
54440	1.79 ± 0.07	27 ± 4	12.35 ± 0.14	8.79 ± 0.10
60070	1.54 ± 0.10	25 ± 4	12.17 ± 0.18	8.79 ± 0.11

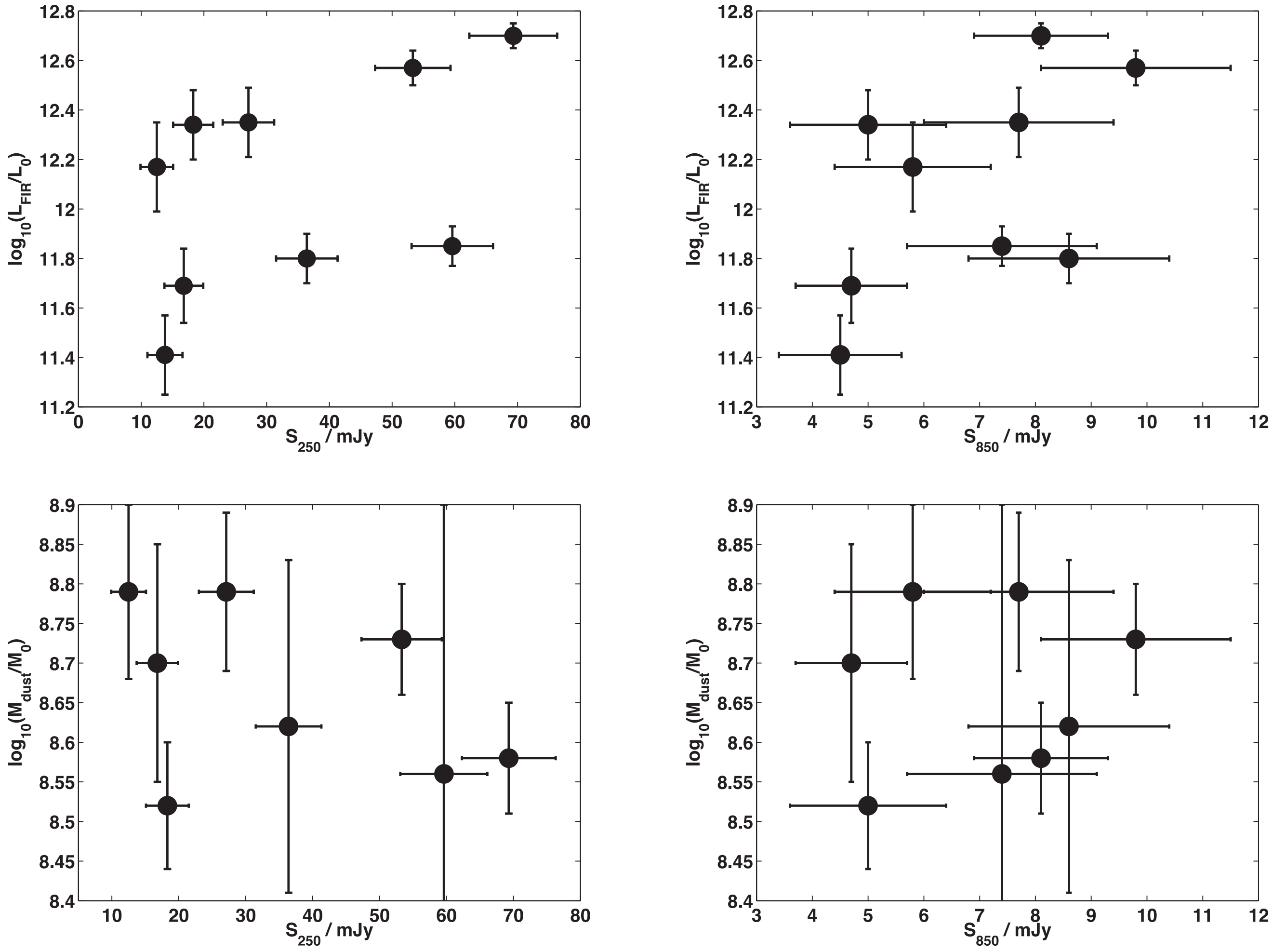

Figure B2. Top: correlation between the far-infrared luminosity estimated from full SED fitting (proxy for star formation) and the 250- and 850-μm fluxes of individually detected AGN. Bottom: correlation between the dust mass estimated from full SED fitting and the 250- and 850-μm fluxes of individually detected AGN.

APPENDIX C: REDSHIFT AND X-RAY LUMINOSITY DISTRIBUTIONS

Here, we present the redshift and hard X-ray luminosity distributions for the various sub-samples that have been stacked in this analysis. These distributions are shown in Figs C1 and C2.

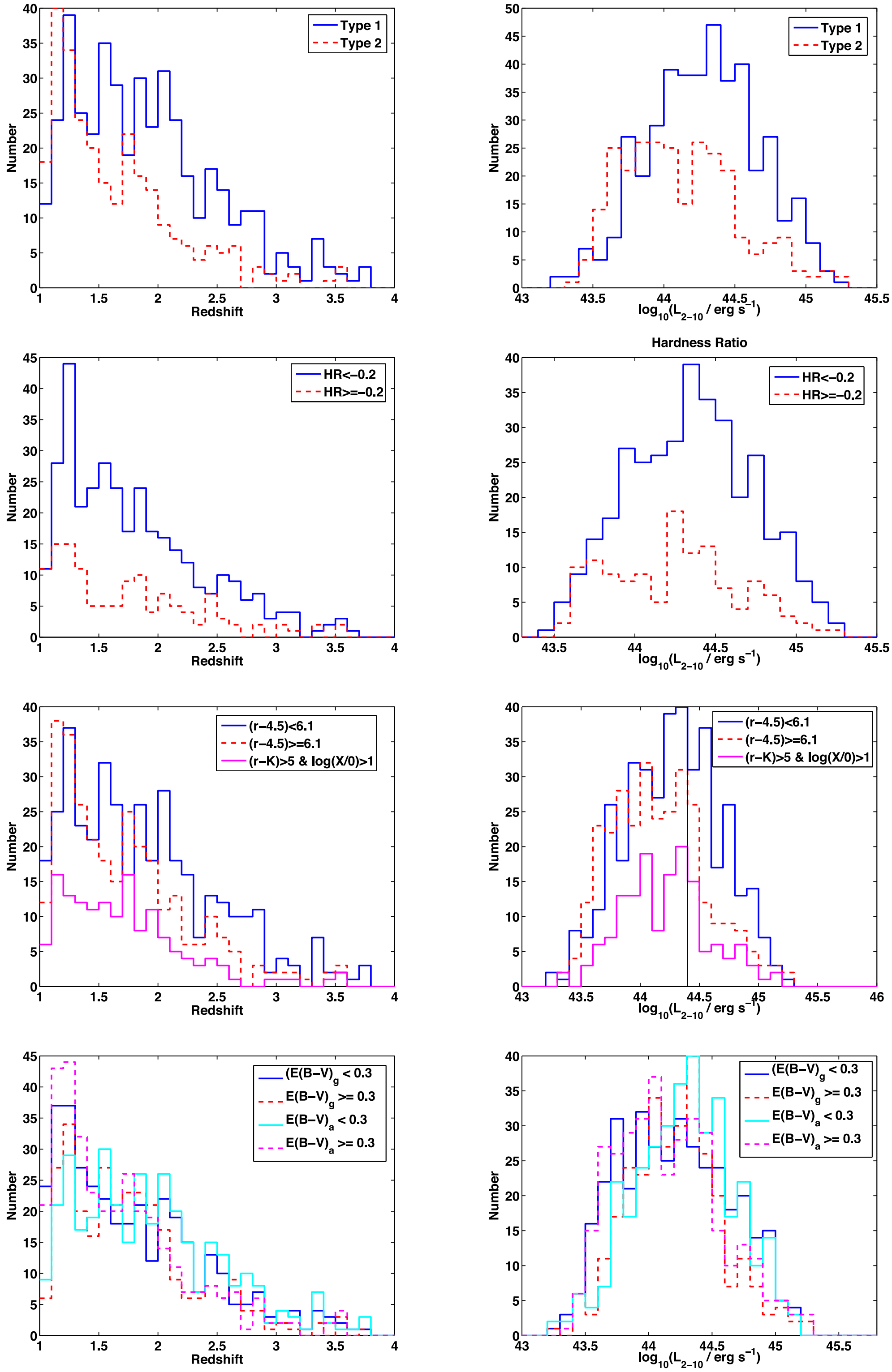

Figure C1. Redshift (left) and X-ray luminosity (right) distributions for various sub-samples of AGN compared in this work. The top panels show AGN separated as type 1 and type 2, the second panels show AGN separated based on HR, the third panels show AGN separated on the basis of optical-to-infrared colours and the bottom panels show AGN separated on the basis of best-fitting dust extinctions. In the third panel, the vertical line marks the X-ray luminosity threshold of $\log_{10}(L_{2-10}) > 44.4$ considered in Section 4.4.

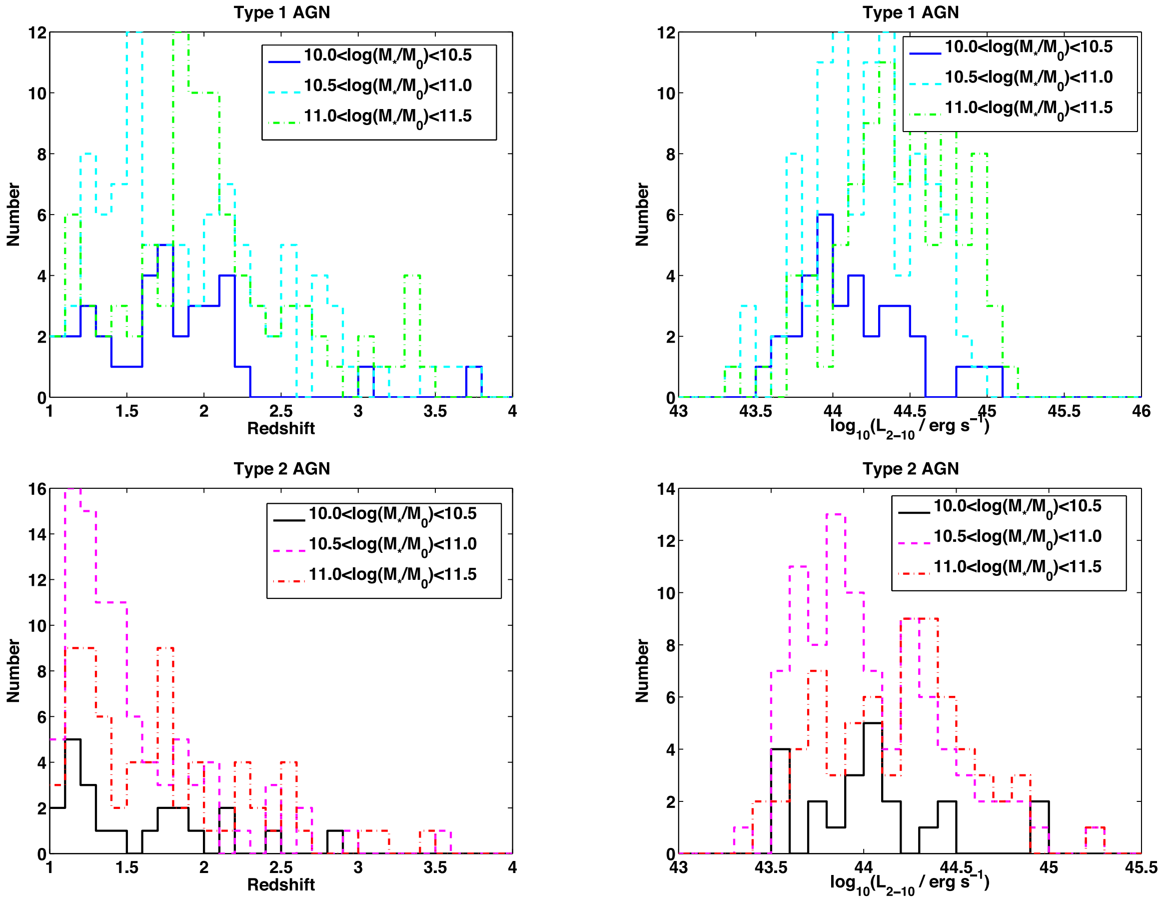

Figure C2. Redshift (left) and X-ray luminosity (right) distributions for the type 1 and type 2 AGN split into the three stellar mass bins considered in Section 4.5.

This paper has been typeset from a TEX/LATEX file prepared by the author.